

In the format provided by the authors and unedited.

# Non-chemisorbed gold-sulfur binding prevails in self-assembled monolayers

Michael S. Inkpen<sup>1\*</sup>, Zhen-Fei Liu<sup>2</sup>, Haixing Li<sup>1</sup>, Luis M. Campos<sup>3</sup>, Jeffrey B. Neaton<sup>2</sup> and Latha Venkataraman<sup>1,3\*</sup>

---

<sup>1</sup>Department of Applied Physics, Columbia University, New York, NY, USA. <sup>2</sup>Molecular Foundry, Lawrence Berkeley National Laboratory and Department of Physics, University of California, Berkeley, Berkeley, CA, USA. <sup>3</sup>Department of Chemistry, Columbia University, New York, NY, USA.

\*e-mail: [inkpen@usc.edu](mailto:inkpen@usc.edu); [lv2117@columbia.edu](mailto:lv2117@columbia.edu)

## Supplementary Information

### Non-chemisorbed gold–sulfur binding prevails in self-assembled monolayers

**Michael S. Inkpen,<sup>\*,†</sup> Zhen-Fei Liu,<sup>§</sup> Haixing Li,<sup>†</sup> Luis M. Campos,<sup>‡</sup> Jeffrey B. Neaton,<sup>§</sup> Latha Venkataraman<sup>\*,†,‡</sup>**

<sup>†</sup>Department of Applied Physics and <sup>‡</sup>Department of Chemistry, Columbia University, New York, New York, United States

<sup>§</sup>Molecular Foundry, Lawrence Berkeley National Laboratory and Department of Physics, University of California, Berkeley, Berkeley, California, United States

### Contents

1. Supplementary Methods	2
2. Supplementary Data	9
3. NMR Spectra	19
4. References	27

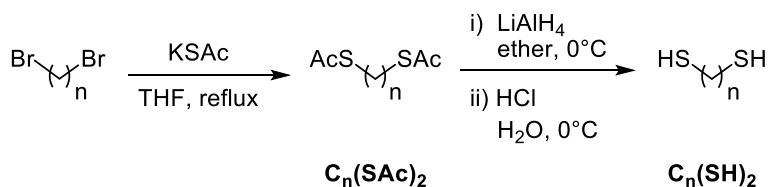
## 1. Supplementary Methods

**STM–BJ details:** Scanning tunnelling microscope–based break junction (STM–BJ) measurements were performed using a custom-built STM that has been described previously.<sup>1</sup> The hardware was controlled using custom software (written using IgorPro, Wavemetrics Inc., OR, USA), and experiments conducted at room temperature under ambient conditions. STM tips were prepared from freshly cut Au wire ( $\varnothing = 0.25$  mm, 99.998%, Alfa Aesar), with substrates for solution measurements prepared from evaporation of  $>100$  nm Au ( $\geq 99.95\%$ , Alfa Aesar) at  $\sim 1$  Å/s onto freshly cleaved mica or mechanically polished steel. Tip–substrate distances were controlled with sub-angstrom precision using a single-axis piezoelectric positioner (Nano-P15, Mad City Labs, WI, USA). Applying a bias between the tip and substrate, conductance was measured as a function of tip–substrate displacement (at 40 kHz acquisition rate) as the tip was repeatedly pushed into the substrate to reach a conductance of  $>5 G_0$  (where  $G_0 = 2e^2/h$ ) and then retracted 5–10 nm (at 18 nm/s) to break the contact. The resulting conductance-distance traces were compiled into 1D conductance histograms (using logarithmic bins 100 bins/decade along the conductance axis), or 2D conductance-distance histograms (using bins of 0.0025 nm along the displacement axis and 100 bins/decade along the conductance axis). Traces in 2D histograms were aligned such that displacement = 0 nm where  $G = 0.5 G_0$ . Most probable conductance values for molecules studied here were obtained through Gaussian fits to their corresponding conductance peaks in 1D histograms. Directly before starting a solution measurement, substrates were treated with UV/ozone for 20 min (using a NovaScan PSD UV, Novascan Technologies, Inc., IA, USA), and 1,000 traces collected to check the gold surface was free from contamination.

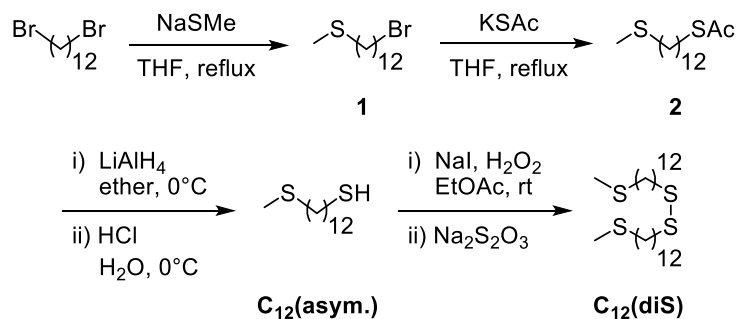
**Preparation of template-stripped gold (TS–Au) substrates:** Following methodologies introduced by others,<sup>2,3</sup> a  $>100$  nm Au layer was evaporated onto 4" Prime Grade  $<100>$  1–10  $\Omega$  cm<sup>-1</sup> 500–550  $\mu\text{m}$  single side polished silicon wafers (Nova Electronic Materials, LLC, Texas, USA). Glass tiles ( $\sim 1$  cm<sup>2</sup>, cleaned using oxygen plasma to improve adhesion) were then bonded to the Au layer (forming a Si-Au-adhesive-glass assembly) using either NOA 61 optical adhesive (Norland Products Inc., New Jersey, USA), or EP41S-5 two-part epoxy (Masterbond, New Jersey, USA). The former was cured through 15 min exposure in a Dymax 400 Watt UV Curing System then aged for  $\geq 12$  h at 50°C, the latter cured for  $\geq 24$  h at room temperature. Immediately prior to use, individual Au-adhesive-glass ensembles were cleaved from the silicon wafer using a razor blade, to reveal a clean, flat Au surface.

**Synthetic procedures:** For an overview, see Supplementary Schemes 1–3 below. All reactions were conducted in oven-dried glassware under a nitrogen or argon atmosphere, though no special precautions were taken to exclude air or moisture during workup and purification. The preparation of **C<sub>n</sub>(SMe)<sub>2</sub>**<sup>4</sup> and **C<sub>7</sub>(SH)<sub>2</sub>**<sup>5,6</sup> followed literature methods. Anhydrous THF was obtained from a Schlenk manifold with purification columns packed with activated alumina and supported copper catalyst (Glass Contour, Irvine, CA). All other materials were commercially available and used as received.

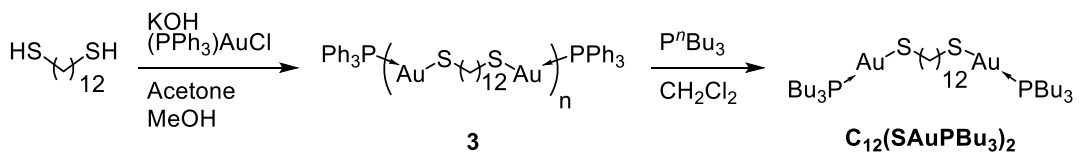
<sup>1</sup>H, <sup>13</sup>C{<sup>1</sup>H} and <sup>31</sup>P{<sup>1</sup>H} NMR spectra were recorded on a Bruker Avance III 400, 400SL (400 MHz), or 500 (500 MHz) spectrometer and referenced to the residual solvent peaks of CD<sub>2</sub>Cl<sub>2</sub> at  $\delta$  5.32 (<sup>1</sup>H) and 53.84 (<sup>13</sup>C{<sup>1</sup>H}) ppm, or externally to 85% phosphoric acid (0.00 ppm). Mass spectrometry analyses were conducted by Brandon Fowler of the Mass Spectrometry Facility, Chemistry Department, Columbia University, New York using a Waters XEVO G2-XS QToF mass spectrometer.



**Supplementary Scheme 1.** General synthetic route for converting alkyl bromides to alkyl thiols.



**Supplementary Scheme 2.** Synthetic route to **C<sub>12</sub>(asym.)** and **C<sub>12</sub>(diS)**.



**Supplementary Scheme 3.** Synthetic route to **C<sub>12</sub>(AuSPBu<sub>3</sub>)<sub>2</sub>**.

**C<sub>12</sub>(SAc)<sub>2</sub>**. This synthesis was adapted from literature methods.<sup>7</sup> Anhydrous THF (63 mL) was added to 1,12-dibromododecane (3.901 g, 11.89 mmol) and potassium thioacetate (3.39 g, 29.68 mmol) in a 100 mL round-bottomed flask equipped with a stirrer bar and condenser. The mixture was heated to reflux with stirring overnight. After cooling to room temperature, volatile components were removed with gentle heating under vacuum. The residue was extracted with CH<sub>2</sub>Cl<sub>2</sub> and filtered through a silica plug. Evaporation of solvent provided **C<sub>12</sub>(SAc)<sub>2</sub>** as a pale-yellow solid (3.754 g, quantitative yield). <sup>1</sup>H NMR (400 MHz, CD<sub>2</sub>Cl<sub>2</sub>):  $\delta$  (ppm) 1.20–1.41 (m, 16H, –CH<sub>2</sub>–), 1.55 (quint., 4H,  $J$  = 7.1 Hz, –CH<sub>2</sub>CH<sub>2</sub>CH<sub>2</sub>SAc), 2.29 (s, 6H, –CH<sub>3</sub>), 2.84 (t, 4H,  $J$  = 7.4 Hz, –CH<sub>2</sub>CH<sub>2</sub>SAc). <sup>13</sup>C{<sup>1</sup>H} NMR (101 MHz, CD<sub>2</sub>Cl<sub>2</sub>):  $\delta$  (ppm) 29.23, 29.49, 29.53, 29.88, 29.95, 29.99, 30.84, 195.98 (C[=O]CH<sub>3</sub>). HRMS (ASAP+): m/z 319.1766 ([M+H]<sup>+</sup> calc. for C<sub>16</sub>H<sub>31</sub>O<sub>2</sub>S<sub>2</sub>: 319.1765).

**C<sub>12</sub>(SH)<sub>2</sub>**. Anhydrous diethyl ether (5 mL) was added to LiAlH<sub>4</sub> (0.5968 g, 15.73 mmol) in a round-bottomed flask equipped with a stirrer bar. A solution of **C<sub>12</sub>(SAc)<sub>2</sub>** (1.025 g, 3.218 mmol) in anhydrous diethyl ether (10 mL) was added dropwise via cannula at 0°C (water–ice bath) with stirring. The suspension was stirred overnight to room temperature, then cooled again to 0°C whereby 2N HCl (7.2 mL) was carefully added dropwise (gas evolution). After stirring for ~10 min, the mixture was filtered through an alumina plug eluting with diethyl ether. After removing solvent *in vacuo*, the crude product was added in a minimum amount of hexanes to a hexanes-packed silica column and eluted with 5–10% CH<sub>2</sub>Cl<sub>2</sub> in hexanes. Evaporation of selected fractions provided **C<sub>12</sub>(SH)<sub>2</sub>** as a white solid (0.683 g, 91%). Note: TLC plates were stained using basic KMnO<sub>4</sub>. <sup>1</sup>H NMR (400 MHz, CD<sub>2</sub>Cl<sub>2</sub>):  $\delta$  (ppm) 1.28 (br s, 12H, –CH<sub>2</sub>–), 1.36 (t, 2H,  $J$  = 7.8 Hz, –SH), 1.37 (br m, 4H, –CH<sub>2</sub>–), 1.59 (quint., 4H,  $J$  = 7.4 Hz, –CH<sub>2</sub>CH<sub>2</sub>CH<sub>2</sub>SH), 2.51 (quart., 4H,  $J$  = 7.2 Hz, –CH<sub>2</sub>CH<sub>2</sub>SH). <sup>13</sup>C{<sup>1</sup>H} NMR (101 MHz, CD<sub>2</sub>Cl<sub>2</sub>):  $\delta$  (ppm) 24.98, 28.81, 29.51, 29.94, 29.99, 34.57. HRMS (ASAP–): m/z 233.1394 ([M–H]<sup>–</sup> calc. for C<sub>12</sub>H<sub>25</sub>S<sub>2</sub>: 233.1398).

**1-Bromo-12-(methylthio)dodecane (1)**. The same methodology as for **C<sub>12</sub>(SAc)<sub>2</sub>** was applied, using anhydrous THF (65 mL), 1,12-dibromododecane (4.040 g, 12.31 mmol) and sodium thiomethoxide (0.841 g, 12.0 mmol). After filtration through a silica plug and removal of solvent *in vacuo*, the crude product was preabsorbed on silica. This was purified by chromatography on a silica column packed with hexanes, eluting with 0–40% CH<sub>2</sub>Cl<sub>2</sub> in hexanes. Evaporation of selected fractions provided the pure product as a pale-yellow liquid (1.073 g, 30%). Note: TLC plates were stained using basic KMnO<sub>4</sub>. <sup>1</sup>H NMR (500 MHz, CD<sub>2</sub>Cl<sub>2</sub>):  $\delta$  (ppm) 1.28 (s, 12H, –CH<sub>2</sub>–), 1.37 (m, 2H, –CH<sub>2</sub>–), 1.41 (m, 2H, –CH<sub>2</sub>–), 1.57 (quint., 2H,  $J$  = 7.7 Hz, –CH<sub>2</sub>CH<sub>2</sub>CH<sub>2</sub>SMe), 1.85 (quint., 2H,  $J$  = 7.3 Hz, –CH<sub>2</sub>CH<sub>2</sub>CH<sub>2</sub>Br),

2.07 (s, 3H,  $CH_3$ ), 2.47 (t, 2H,  $J$  = 7.1 Hz,  $-CH_2CH_2SMe$ ), 3.42 (t, 2H,  $J$  = 6.9 Hz,  $-CH_2CH_2Br$ ).  $^{13}C\{^1H\}$  NMR (126 MHz,  $CD_2Cl_2$ ):  $\delta$  (ppm) 15.60, 28.57, 29.16, 29.22, 29.63, 29.65, 29.84, 29.92, 29.93, 29.95, 33.32, 34.60, 34.68. HRMS (ASAP+): m/z 297.1072 ([M+H]<sup>+</sup> calc. for  $C_{13}H_{28}BrS$ : 297.1075).

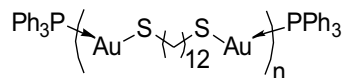
**1-(Acetylthio)-12-(methylthio)dodecane (2).** The same methodology as for **C<sub>12</sub>(SAc)<sub>2</sub>** was applied, using anhydrous THF (18 mL), **1** (1.01 g, 3.42 mmol) and potassium thioacetate (1.029 g, 9.01 mmol). After filtration through a silica plug and removal of solvent *in vacuo*, the crude product was obtained as a pale-yellow solid (1.032 g, quantitative yield).  $^1H$  NMR (500 MHz,  $CD_2Cl_2$ ):  $\delta$  (ppm) 1.27 (s, 12H,  $-CH_2-$ ), 1.36 (m, 4H,  $-CH_2-$ ), 1.56 (m, 4H,  $-CH_2-$ ), 2.07 (s, 3H,  $-SCH_3$ ), 2.29 (s, 3H,  $-SC[=O]CH_3$ ), 2.47 (t, 2H,  $J$  = 7.4 Hz,  $-CH_2CH_2SMe$ ), 2.84 (t, 2H,  $J$  = 7.3 Hz,  $-CH_2CH_2SAc$ ).  $^{13}C\{^1H\}$  NMR (126 MHz,  $CD_2Cl_2$ ):  $\delta$  (ppm) 15.60, 29.21, 29.23, 29.48, 29.52, 29.64, 29.66, 29.88, 29.95, 29.97, 30.83, 34.60, 196.02 ( $-C[=O]CH_3$ ). HRMS (ASAP+): m/z 291.1818 ([M+H]<sup>+</sup> calc. for  $C_{15}H_{31}OS_2$ : 291.1816).

**C<sub>12</sub>(asym.).** The same methodology as for **C<sub>12</sub>(SH)<sub>2</sub>** was applied, using anhydrous diethyl ether (5 mL) and LiAlH<sub>4</sub> (0.194 g, 5.11 mmol), then **2** (0.55 g, 1.895 mmol), anhydrous diethyl ether (15 mL), and 2N HCl (2.16 mL). After removing solvent *in vacuo*, the crude product was added in a minimum amount of hexanes to a hexanes-packed silica column and eluted with 20%  $CH_2Cl_2$  in hexanes. Evaporation of selected fractions provided the pure product as a colourless liquid (0.408 g, 87%). Note: TLC plates were stained using basic KMnO<sub>4</sub>.  $^1H$  NMR (500 MHz,  $CD_2Cl_2$ ):  $\delta$  (ppm) 1.28 (s, 12H,  $-CH_2-$ ), 1.36 (t, 1H,  $J$  = 7.8 Hz,  $-SH$ ), 1.37 (m, 4H,  $-CH_2-$ ), 1.58 (m, 4H,  $-CH_2CH_2CH_2SR$ ), 2.07 (s, 3H,  $-SCH_3$ ), 2.49 (m, 4H,  $-CH_2CH_2SR$ ).  $^{13}C\{^1H\}$  NMR (126 MHz,  $CD_2Cl_2$ ):  $\delta$  (ppm) 15.59, 24.96, 28.78, 29.22, 29.48, 29.62, 29.65, 29.92, 29.94, 29.97, 29.97, 34.55, 34.59. HRMS (ASAP-): m/z 247.1552 ([M-H]<sup>-</sup> calc. for  $C_{13}H_{27}S_2$ : 247.1554).

**C<sub>12</sub>(diS).** This synthetic route was adapted from an analogous procedure.<sup>8</sup> In an open flask, hydrogen peroxide (30 wt. % in  $H_2O$ , 0.07 mL, 0.7 mmol) was added with stirring to **C<sub>12</sub>(asym.)** (0.150 g, 0.604 mmol) and sodium iodide (0.001 g, 0.007 mmol) in ethyl acetate (2 mL). After stirring in air for 0.5 h at 20°C, the yellow-brown mixture was poured into saturated *aq.*  $Na_2S_2O_3$  (~10 mL). The aqueous layer was extracted with ethyl acetate (3 x ~20 mL), and the combined organic phase dried over  $Na_2SO_4$ , filtered and solvent removed in *vacuo*. The crude material was purified via chromatography using a silica column packed with hexanes, eluting with 0–20%  $CH_2Cl_2$  in hexanes. Evaporation of selected fractions provided the pure product as a white crystalline solid (0.084 g, 56%).  $^1H$  NMR (500 MHz,  $CD_2Cl_2$ ):  $\delta$

(ppm) 1.28 (br s, 24H,  $-CH_2-$ ), 1.37 (br s, 8H,  $-CH_2-$ ), 1.57 (quint., 4H,  $J = 7.6$  Hz,  $-CH_2CH_2CH_2SMe$ ), 1.66 (quint., 4H,  $J = 7.5$  Hz,  $-CH_2CH_2CH_2SS-$ ), 2.07 (s, 6H,  $-SCH_3$ ), 2.47 (t, 4H,  $J = 7.4$  Hz,  $-CH_2CH_2SMe$ ), 2.68 (t, 4H,  $J = 7.3$  Hz,  $-CH_2CH_2SS-$ ).  $^{13}C\{^1H\}$  NMR (126 MHz,  $CD_2Cl_2$ ):  $\delta$  (ppm) 15.61, 28.91, 29.24, 29.64, 29.67, 29.92, 29.96, 29.99, 30.00, 34.61, 39.58, 54.06. HRMS (ASAP+): m/z 247.1544 ( $[M_{\text{fragment}}]^+$  calc. for  $C_{13}H_{27}S_2$ : 247.1554), 494.3109 ( $[M+H]^+$  calc. for  $C_{26}H_{54}S_4$ : 494.3108).

**$C_{12}(SAuPBu_3)_2$ .** This synthetic route was based upon previous work with related systems (Supplementary Scheme 3).<sup>9,10</sup> A solution of KOH in methanol (0.015 g in 1 mL, 0.27 mmol) was added to a mixture of  $C_{12}(SH)_2$  (0.029 g, 0.124 mmol) and chloro(triphenylphosphine)gold(I) (0.135 g, 0.273 mmol) in acetone (5 mL). After stirring for 1 h, solvent was removed *in vacuo*. The residue was washed with MeOH (3 x ~15 mL) and  $CH_2Cl_2$  (25 mL) to provide **3** as a white solid (0.053 g) which was insoluble in most organic solvents including MeOH,  $CH_2Cl_2$  and DMSO. The polymeric nature of this material as shown in the below structure is suggested based on its poor solubility. Traces of triphenylphosphine were observed by NMR when samples were solubilized with  $P^nBu_3$  (see below and Supplementary Figures 23, 25).



Tri-*n*-butylphosphine (0.02 mL) was added to a suspension of **3** (0.009 g) in  $CH_2Cl_2$  (3 mL), and the mixture stirred at room temperature for 30 min. All solid material rapidly dissolved to provide a colourless solution. This solution was diluted in 1,2,4-trichlorobenzene for use directly in STM–BJ experiments. Comparisons between NMR spectra for  $C_{12}(SAuPBu_3)_2$ , free  $C_{12}(SH)_2$  and  $P^nBu_3$  are shown in Supplementary Figures 23–25.  $^1H$  NMR (400 MHz,  $CD_2Cl_2$ ):  $\delta$  (ppm) 1.27 (br s, 12H,  $-CH_2-$  in  $C_{12}$ ), 1.63 (quint. 4H,  $-CH_2CH_2CH_2SAu-$ ), 2.84 (t, 4H,  $J = 7.3$  Hz,  $-CH_2CH_2SAu-$ ), other resonances overlap with those attributable to  $P^nBu_3$ .  $^{31}P\{^1H\}$  NMR (162 MHz,  $CD_2Cl_2$ ):  $\delta$  (ppm) -11.15 (br s,  $-AuP^nBu_3$ ). HRMS (ES+): m/z 1031.4435 ( $[M+H]^+$  calc. for  $C_{36}H_{80}Au_2P_2S_2$ : 1031.4430).

**$Ph_3(SAuPPh_3)_2$ .** The title compound was prepared via the literature procedure.<sup>11</sup> Spectroscopic and mass spectrometric features matched reported values. Comparisons between NMR spectra for  $Ph_3(SAuPPh_3)_2$ , free *p*-terphenyl-4,4-dithiol  $Ph_3(SH)_2$  and  $PPh_3$  are shown in Supplementary Figures 26–28.

**Computational details:** We use a trimer motif or a gold adatom to bind the S atoms to the Au electrodes. A total of twelve junctions are relaxed:  $C_n(SH)_2$ ,  $C_n(SMe)_2$ , and  $C_nS_2$ , respectively,

with  $n = 4, 8$ , (trimer only) and  $12$  (trimer and gold adatom), respectively. To make the local binding geometries similar in all nine junctions using the trimer motif, we first optimize the junction for the longest alkane ( $C_{12}(SMe)_2$ ) on one Au(111) electrode and then use the resulting bond orientation and angle to initiate the relaxation of other systems. We then add the second electrode and run a full geometry relaxation of each junction (with further details below). The final gold–sulfur bond length and its angle relative to the molecular backbone may change after the geometry relaxation, in which the total energy is minimized.

During the geometry relaxation of the junction, the outer four layers of gold on each side are moved together as rigid bodies along the transport ( $z$ ) direction, with forces along  $z$ -direction calculated as an average of all  $z$ -direction forces on the layer farthest from the outmost layer. The internal atomic distances within the four layers are kept at the bulk values. Coordinates of other atoms are allowed to relax fully until forces are below  $0.04$  eV/Å. In this way, we achieve an optimal geometry around the molecule–gold contact, while maintaining bulk gold geometry far away from the molecule. Periodic boundary conditions and a  $4 \times 4 \times 1$  k-mesh are used in the geometry relaxation. A  $0.02$  eV effective electronic temperature is used to smear the Fermi–Dirac distribution function. Supplementary Figure 6 shows the relaxed geometries for the  $C_4$  series. The gold–sulfur bond lengths in alkanes bound through physisorbed bonds (Au–S(H)R or Au–S(Me)R) are about  $2.5$ – $2.55$  Å while they are about  $2.35$ – $2.4$  Å for the chemisorbed alkanes.

**XPS measurements:** X-ray photoelectron spectra were recorded on a PHI 5500 model spectrometer equipped with a MgK $\alpha$  standard (non-monochromated) X-ray source, hemispherical electron energy analyzer, and multichannel detector. Spectra were acquired using a  $15$  kV anode potential and  $13.3$  mA emission current (X-ray source power =  $200$  Watts), with an analyser pass energy of  $23.50$  eV. The surface normal-detector take off angle was  $15^\circ$ , and chamber pressures during measurements were maintained at  $\leq 1 \times 10^{-9}$  Torr. Binding energy scales for each sample were referenced to the Au  $4f_{7/2}$  peak at  $84.00$  eV. Spectra were obtained by averaging  $10$  consecutive scans to improve the signal-to-noise ratio.

**Electrochemical measurements:** Electrochemical measurements were carried out using a  $\mu$ AutolabIII potentiostat (MetroOhm Autolab B.V., Utrecht, The Netherlands) in  $0.1$  M KOH aqueous solution with a SAM-functionalized gold wire working electrode ( $\varnothing = 0.25$  mm, 99.998%, Alfa Aesar) at a scan rate of  $50$  mV/s. We used Ag/AgCl reference and Pt counter electrodes, and report potentials relative to Ag/AgCl. Gold wires were flame annealed using a

butane torch immediately prior to SAM formation. SAMs were formed on these gold wires using the same procedure as for the STM–BJ measurements (see Methods).

## 2. Supplementary Data

**Supplementary Table 1.** Overview of primary conductance experiments.<sup>a</sup>

entry	analyte	$G_{\text{Sol.}} (G_0)^b$	$G_{\text{SAM}} (G_0)^c$
1	$\mathbf{C_2(SH)_2}$	*	$1.4 \times 10^{-2}$
2	$\mathbf{C_4(SH)_2}$	*	$2.6 \times 10^{-3}$
3	$\mathbf{C_6(SH)_2}$	$5.4 \times 10^{-4}$	$3.3 \times 10^{-4}$
4	$\mathbf{C_7(SH)_2}$	$2.0 \times 10^{-4}$	$1.2 \times 10^{-4}$
5	$\mathbf{C_8(SH)_2}$	$9.0 \times 10^{-5}$	$5.3 \times 10^{-5}$
6	$\mathbf{C_9(SH)_2}$	$5.2 \times 10^{-5}$	$2.3 \times 10^{-5}$
7	$\mathbf{C_{10}(SH)_2}$	$2.4 \times 10^{-5}$	$7.7 \times 10^{-6}$
8	$\mathbf{C_{12}(SH)_2}$	$3.3 \times 10^{-6}$	$9.0 \times 10^{-7}$
9	$\mathbf{C_4(SMe)_2}$	$1.6 \times 10^{-3}$	-
10	$\mathbf{C_8(SMe)_2}$	$4.3 \times 10^{-5}$	-
11	$\mathbf{C_{12}(SMe)_2}$	$9.1 \times 10^{-7}$	$9.7 \times 10^{-7}$
12	$\mathbf{C_{12}(SAuPBu_3)_2}$	$3.0 \times 10^{-6}$	-
13	$\mathbf{C_{12}(asym.)}$	$1.5 \times 10^{-6}$	$1.0 \times 10^{-6}$
14	$\mathbf{C_{12}(diS)}$	$1.6 \times 10^{-6}$	$8.0 \times 10^{-7}$
15	$\mathbf{Ph_3(SH)_2}$	$1.9 \times 10^{-3}$	$8.2 \times 10^{-4}^d$
16	$\mathbf{Ph_3(SMe)_2}$	$7.7 \times 10^{-4}$	-
17	$\mathbf{Ph_3(SAuPPh_3)_2}$	$2.0 \times 10^{-3}$	-

<sup>a</sup> Conductance cell colours correlate with relevant manuscript and SI figure plots. Entry: 1–8 = alkanedithiols [ $\mathbf{C_n(SH)_2}$ ]; 9–11 = alkanedithiomethyls [ $\mathbf{C_n(SMe)_2}$ ]; 12–14 = 1,12-dodecane backbone ( $\mathbf{C_{12}}$ ) species with different sulfur linker groups; 15–17 = terphenyl backbone ( $\mathbf{Ph_3}$ ) species with different sulfur linker groups. Starred cells indicate conductance peak for that measurement is ill-defined and cannot be fit reliably. Dashed cells indicate experiment not performed. <sup>b</sup> Solution measurement, 0.1 mM in TCB. <sup>c</sup> SAM measurement, with SAMs prepared from a 1 mM EtOH solution. <sup>d</sup> SAM measurement, with SAMs prepared from a 0.05 mM EtOH solution.

**Supplementary Table 2.** Overview of solution measurement control experiments.<sup>a</sup>

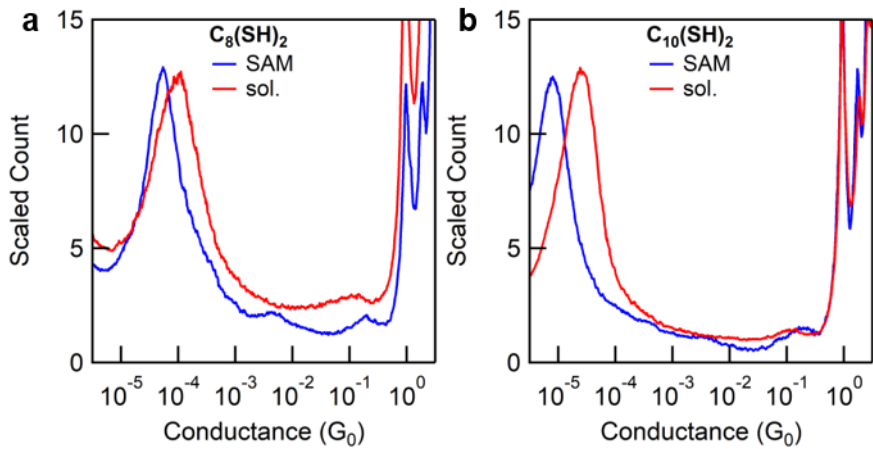
entry	analyte	solvent	conc. (mM)	bias (mV)	G (G <sub>0</sub> )
18	<b>C<sub>12</sub>(SH)<sub>2</sub></b>	TCB	0.01	345	3.1 × 10 <sup>-6</sup>
19	<b>C<sub>12</sub>(asym.)</b>	TCB	0.01	345	1.7 × 10 <sup>-6</sup>
20	<b>C<sub>12</sub>(SMe)<sub>2</sub></b>	TCB	0.01	345	9.1 × 10 <sup>-7</sup>
21	<b>C<sub>10</sub>(SH)<sub>2</sub></b>	tetradecane	0.1	230	1.8 × 10 <sup>-5</sup>
22	<b>C<sub>10</sub>(SH)<sub>2</sub></b>	isopropanol	0.1	230	2.1 × 10 <sup>-5</sup>
23	<b>C<sub>10</sub>(SH)<sub>2</sub></b>	isopropanol	0.1	-230	2.1 × 10 <sup>-5</sup>

<sup>a</sup> Conductance cell colours correlate with relevant Supplementary Figure plots. Entry: 18–20 = concentration; 21–23 = solvent, bias polarity.

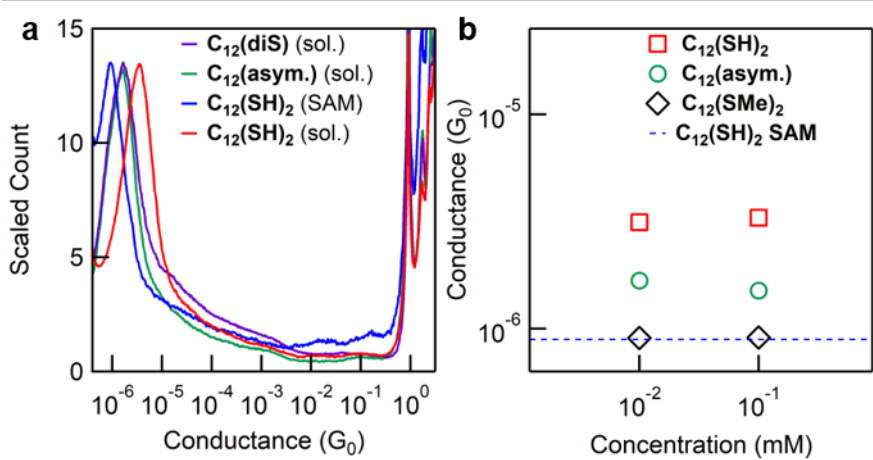
**Supplementary Table 3.** Overview of SAM measurement control experiments.<sup>a</sup>

entry	analyte	substrate	time <sup>b</sup>	solvent <sup>c</sup>	Bias (mV)	G (G <sub>0</sub> )
24	<b>C<sub>10</sub>(SH)<sub>2</sub></b>	TS–Au	1 d	toluene	230	8.9 × 10 <sup>-6</sup>
25	<b>C<sub>10</sub>(SH)<sub>2</sub></b>	Au-on-steel	1 d	EtOH	230	9.6 × 10 <sup>-6</sup>
26	<b>C<sub>10</sub>(SH)<sub>2</sub></b>	Au-on-steel	1 d	EtOH (TCB) <sup>d</sup>	230	9.7 × 10 <sup>-6</sup>
27	<b>C<sub>12</sub>(SH)<sub>2</sub></b>	TS–Au	1 min	EtOH	345	*
28	<b>C<sub>10</sub>(SH)<sub>2</sub></b>	TS–Au	1 h	EtOH	230	7.7 × 10 <sup>-6</sup>
29	<b>C<sub>10</sub>(SH)<sub>2</sub></b>	TS–Au	1 h	EtOH (Ar) <sup>e</sup>	230	8.2 × 10 <sup>-6</sup>
30	<b>C<sub>12</sub>(SH)<sub>2</sub></b>	TS–Au	1 d	EtOH	345	1.2 × 10 <sup>-6</sup>
31	<b>C<sub>12</sub>(SH)<sub>2</sub></b>	TS–Au	1 d	EtOH	-345	1.2 × 10 <sup>-6</sup>

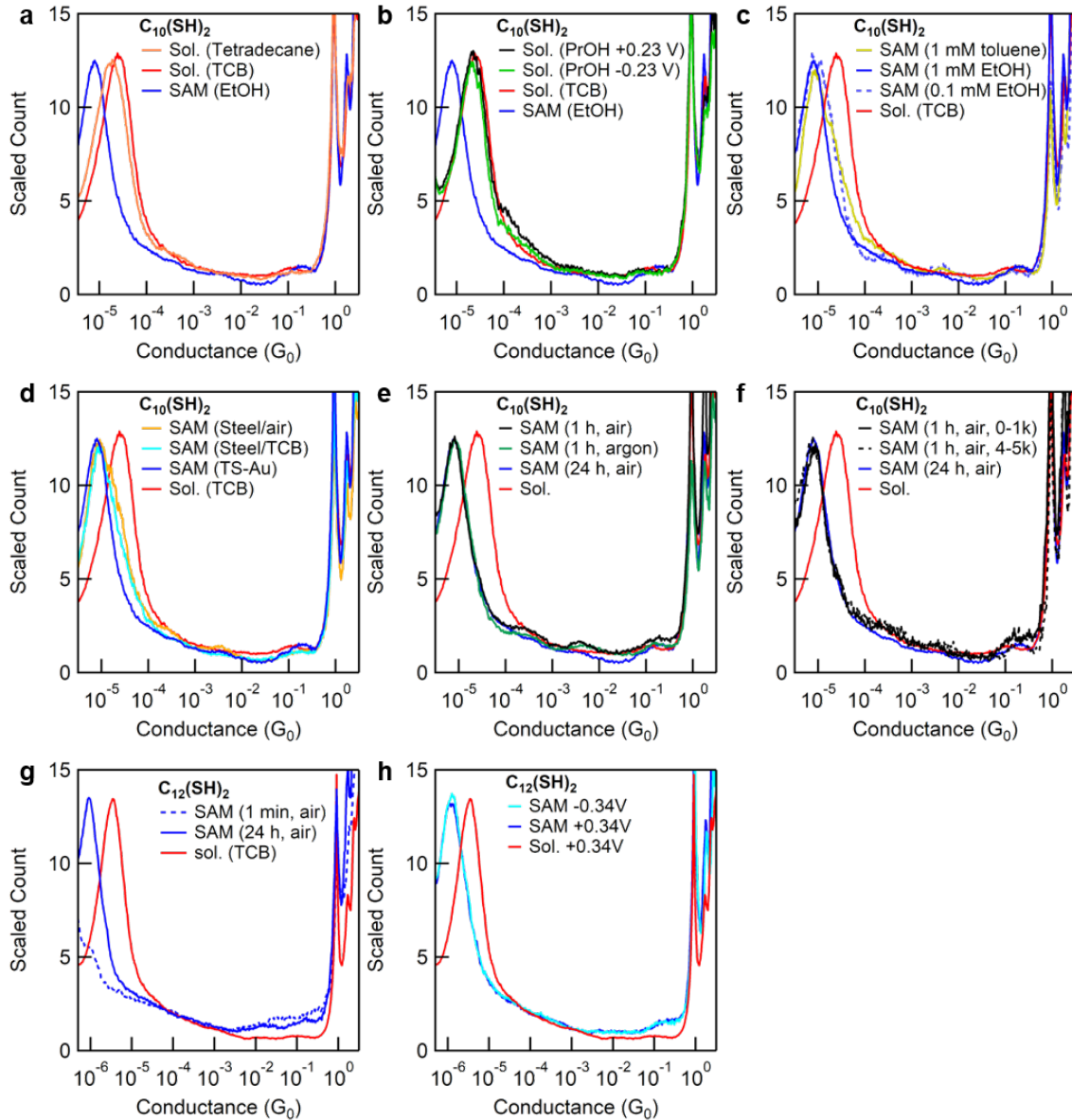
<sup>a</sup> STM–BJ measurements were performed on SAMs in air unless otherwise stated. No effort to exclude oxygen during SAM preparation was made unless otherwise stated. Entry: 24 = solvent used in SAM preparation; 25–26 = substrate roughness and solution environment; 27–29 = preparation time and effect of oxygen; 30–31 = bias polarity (both datasets measured at the same day on the same substrate, with the bias polarity alternated from trace to trace). Starred cells indicate conductance peak for that measurement is ill-defined and cannot be fit reliably. <sup>b</sup> Time substrate immersed in solution to prepare the SAM, where ‘1 d’ = 18–28 h. <sup>c</sup> Solvent used to make the solution that the substrate was immersed in, unless otherwise stated. <sup>d</sup> TCB added on top of the SAM. <sup>e</sup> SAM prepared under argon, using an argon-sparged solution.



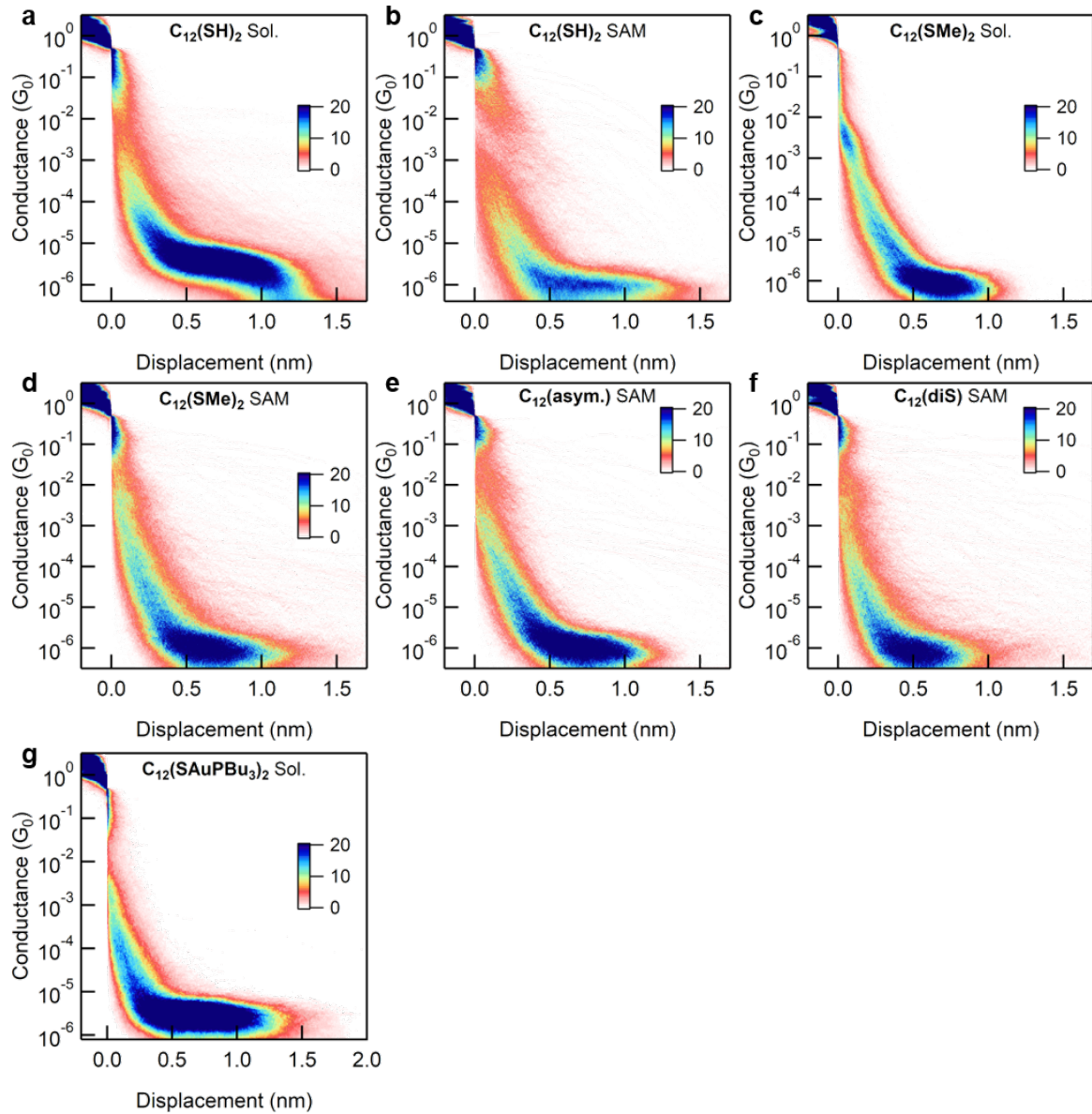
**Supplementary Figure 1.** Overlaid one-dimensional conductance histograms for (a)  $\text{C}_8(\text{SH})_2$  and (b)  $\text{C}_{10}(\text{SH})_2$  solution (10,000 traces/histogram) and SAM (5,000 traces) measurements at  $V_{\text{bias}} = 230$  mV. Histograms from solution measurements are scaled to have comparable peak heights by factors ranging from 0.7–1.2.



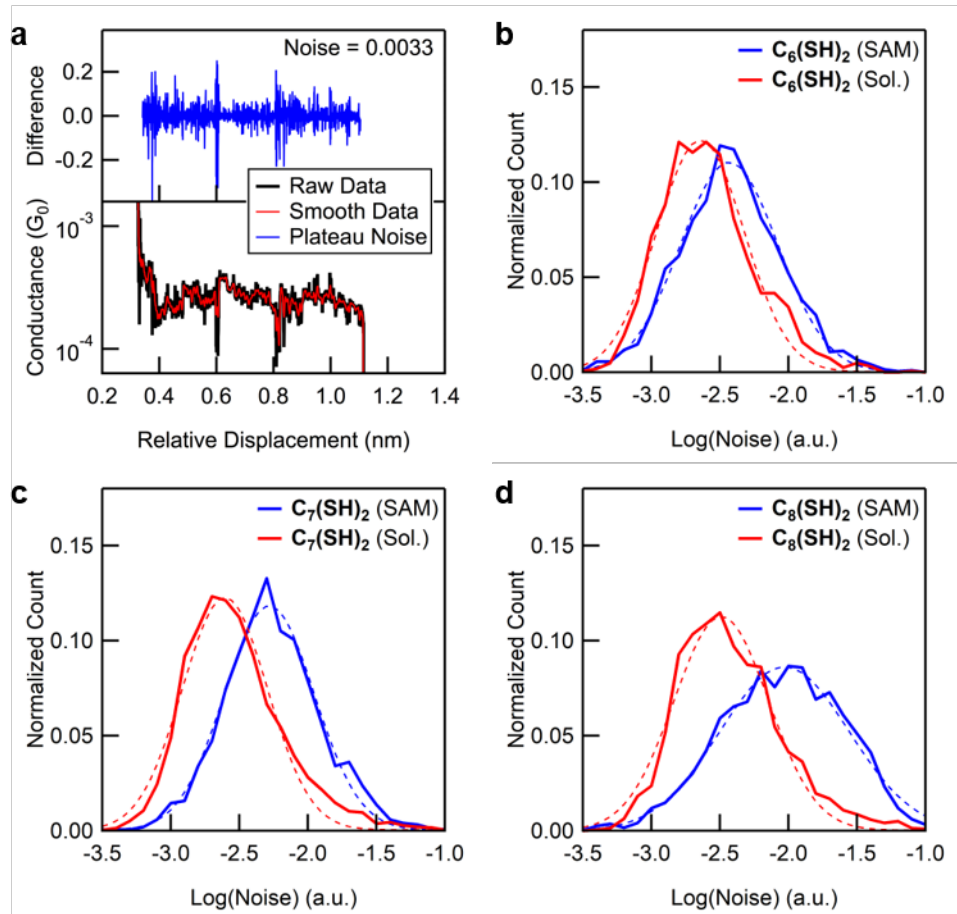
**Supplementary Figure 2.** (a) Overlaid one-dimensional histograms for asymmetrically substituted  $\text{C}_{12}$ -alkanes  $\text{C}_{12}(\text{diS})$  and  $\text{C}_{12}(\text{asym.})$  (structures in manuscript **Figure 1d**) solution measurements (345 mV, 10,000 traces), showing that their conductance is intermediate between that of  $\text{C}_{12}(\text{SH})_2$  SAM (physisorbed bonds on both sides) and solution (chemisorbed bonds on both sides) measurements. Histograms are scaled relative to the  $\text{C}_{12}(\text{SH})_2$  SAM measurement (solid blue line) to have comparable peak heights, by factors ranging from 0.6–1.1. (b) The conductance histogram peak values of different  $\text{C}_{12}$ -alkane solution measurements at different concentrations compared with  $\text{C}_{12}(\text{SH})_2$  SAM measurements (dashed blue line). This shows solution concentration does not explain the lower conductance observed for components in SAM measurements.



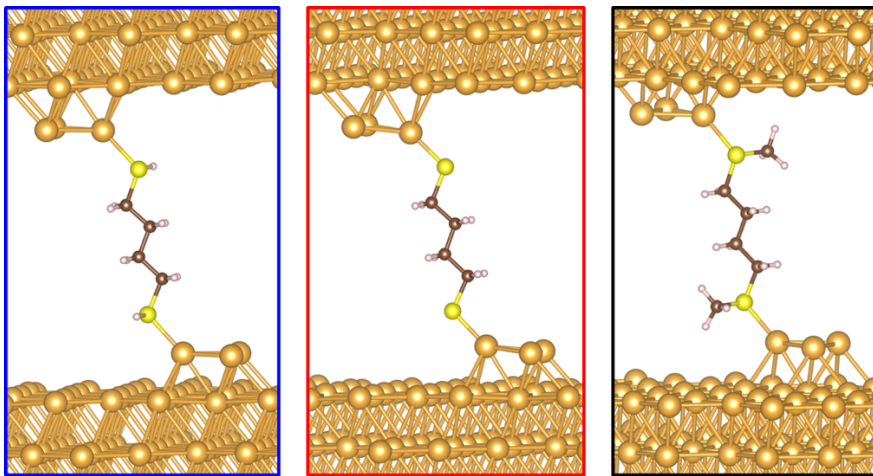
**Supplementary Figure 3.** Overlaid one-dimensional conductance histograms for C<sub>10</sub>(SH)<sub>2</sub> or C<sub>12</sub>(SH)<sub>2</sub> measured under different conditions: solution measurements in **(a)** tetradecane and **(b)** propanol; **(c)** SAM measurements using SAMs prepared from 1 mM toluene or 0.1 mM EtOH solutions; **(d)** SAM measurements using a rough Au surface (Au evaporated onto a mechanically polished steel substrate), and with TCB on top of the SAM; **(e)** SAM measurements using SAMs prepared by immersion in an ethanol solution for different times, and in an argon environment; **(f)** additional analysis of SAM measurements from **(e)** [1 h, air] where the first and last 1000 traces are plotted and **(g)** a SAM measurement of a SAM prepared by immersion in an ethanol solution for a very short time, showing there is no significant conductance change/SAM bonding evolution on the measurement timescale (~2-4 h); **(h)** SAM measurements at different biases. Histograms are scaled relative to the standard C<sub>n</sub>(SH)<sub>2</sub> SAM measurement in each figure (solid blue line) to have comparable peak heights, by factors ranging from 0.7–1.3. Note that the conductance of SAM measurements never reaches that of solution measurements for the same molecule.



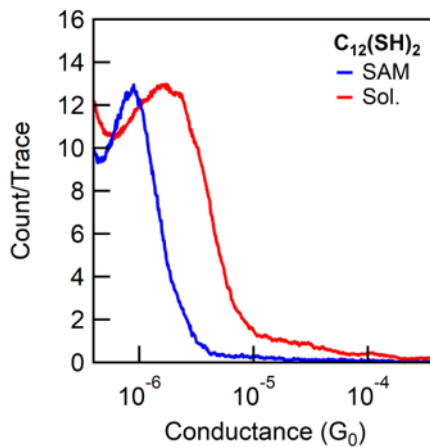
**Supplementary Figure 4.** Two-dimensional conductance histograms for all data shown in Figure 1 of the manuscript. They are created by aligning all measured traces to zero displacement at  $0.5 G_0$  and using 100 bins/decade along the conductance axis and 400 bins/nm along the displacement axis. Each is compiled, without data selection, from 5,000 conductance traces measured at an applied bias of 345 mV.



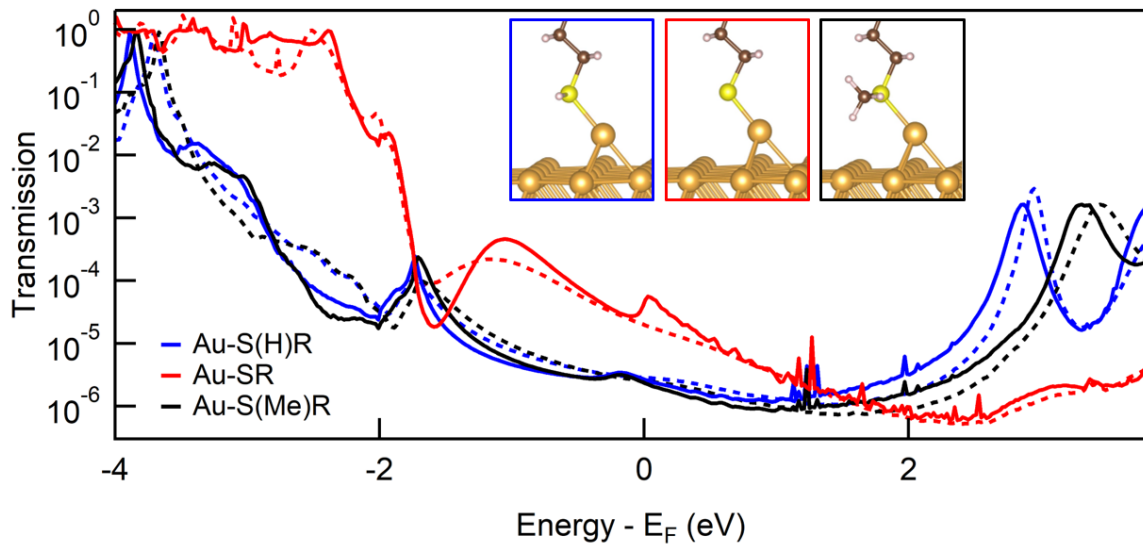
**Supplementary Figure 5.** **(a)** Example trace demonstrating how the average noise is extracted from an individual plateau. The plateau region is first selected and the raw data is smoothed (by averaging 11 neighbouring points). The differences between the raw and smooth data for all the points that comprise the plateau are computed (upper panel). These differences are squared and their sum for each trace is normalized by the number of points in the selected segment, to yield 0.0033 for the trace shown. Noise histograms are subsequently prepared using these average plateau noise values using logarithm bins for the selected traces within a given dataset. **(b)–(d)** Overlaid normalized histograms of the average plateau noise for molecules with  $C_n(SH)_2$  backbones for  $n = 6, 7$ , and  $8$  (solid lines) and their Gaussian fits (dotted lines). As discussed in the manuscript and Methods section, in these analyses we select plateaus that fall within the conductance histogram for the corresponding molecule.



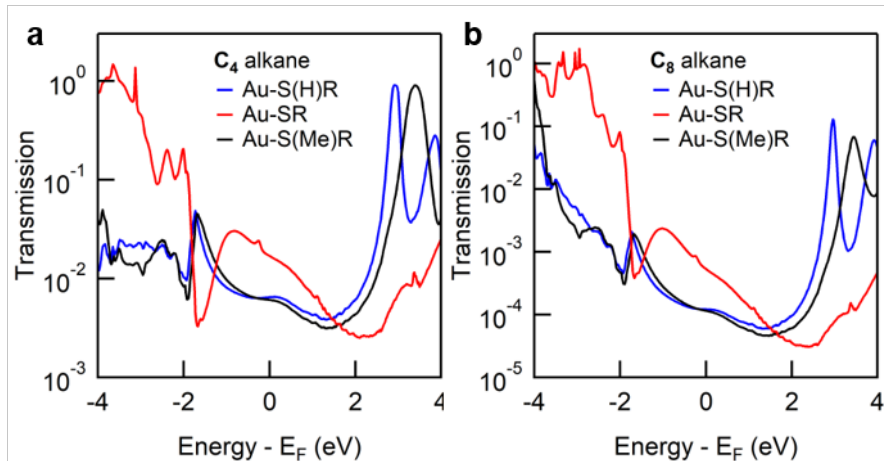
**Supplementary Figure 6.** DFT-optimized junction geometries for  $\mathbf{C_4(SH)_2}$ ,  $\mathbf{C_4(S)_2}$ , and  $\mathbf{C_4(SMe)_2}$ . As shown by others, such a geometry is typical for molecules with physisorbed contacts (such as  $-\text{SMe}$ ,  $-\text{SH}$  or  $-\text{NH}_2$ )<sup>12</sup> and for chemisorbed thiols.<sup>13</sup> To confirm that the trends in our conductance data also hold at maximum junction extension, we present line profile histograms for  $\mathbf{C_{12}(SH)_2}$  in Supplementary Figure 7.



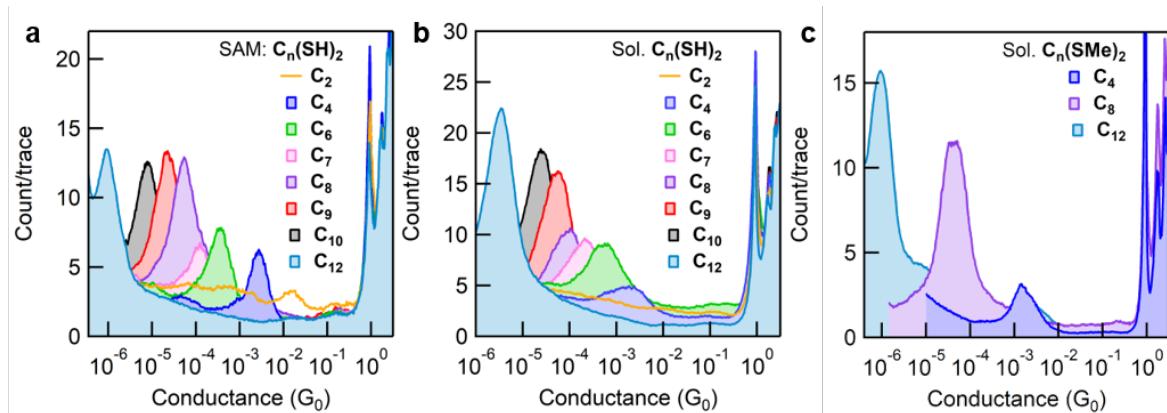
**Supplementary Figure 7.** One-dimensional line profile histograms for  $\mathbf{C_{12}(SH)_2}$ . These are prepared from the 2D histograms shown in Supplementary Figure 4 (using datapoints between 1.2–1.7 nm) for SAM and solution measurements. This analysis provides the average conductance of traces at the point of maximum junction extension, immediately prior to junction rupture. The data clearly shows that under conditions where both chemisorbed and physisorbed molecules are expected to bind to the electrode predominantly through a single gold atom (e.g. trimer motif or adatom), the conductance of thiol-terminated molecules measured in solution is still significantly higher than the conductance measured in a SAM. This further supports our choice of junction geometries for transmission calculations, and our hypothesis that the difference in conductance between solution and SAM measurements of SH-terminated molecules is attributable to differences in the gold–sulfur bonding interaction (i.e. chemisorbed vs physisorbed contact). The histogram from SAM measurements is scaled by a factor of 1.3.



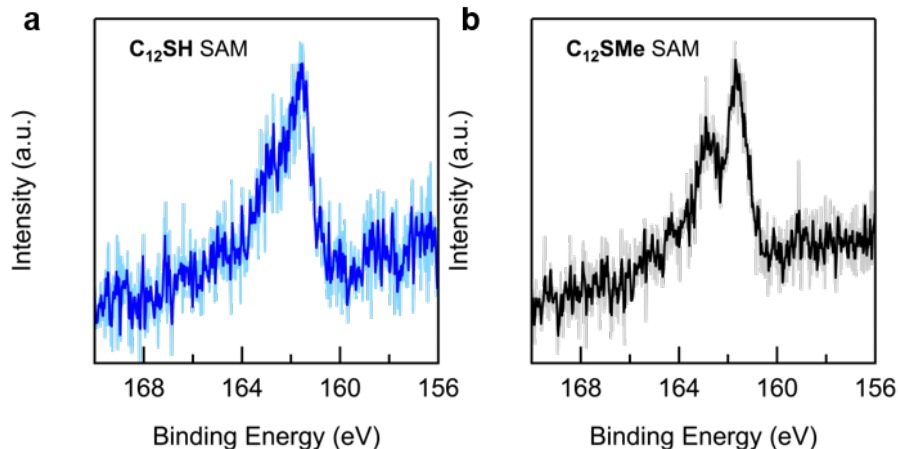
**Supplementary Figure 8.** Calculated transmission functions for  $C_{12}$ -alkanes using an adatom motif on the tip and substrate electrodes (solid lines), with  $Au-S(H)R$  (blue),  $Au-SR$  (red) and  $Au-S(Me)R$  (black) bonds as illustrated in the insets. Calculated transmission functions from Figure 4a for analogous junctions using the trimer gold motif are overlaid (dashed lines), showing that calculations using different  $Au$  junction structures provide the same basic result.



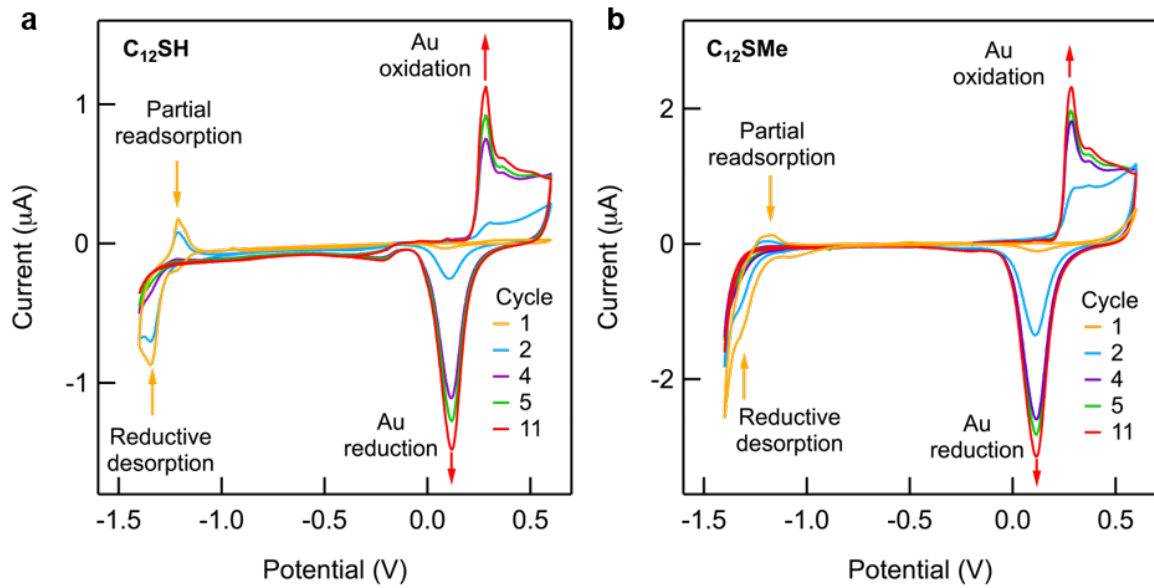
**Supplementary Figure 9.** Transmission versus energy relative to the Fermi energy ( $E_F$ ) for the **(a)**  $C_4$  and **(b)**  $C_8$  series using a gold trimer bonding motif.



**Supplementary Figure 10.** Overlaid one-dimensional conductance histograms for (a)  $C_n(SH)_2$  SAM measurements (5,000 traces/histogram), (b)  $C_n(SH)_2$  solution measurements ( $\geq 8,000$  traces), and (c)  $C_n(SMe)_2$  solution measurements (5,000 traces). All data was obtained at  $V_{bias} = 230$  mV, except for  $C_{12}(SH)_2$  and  $C_n(SMe)_2$  which were measured at 345 mV.

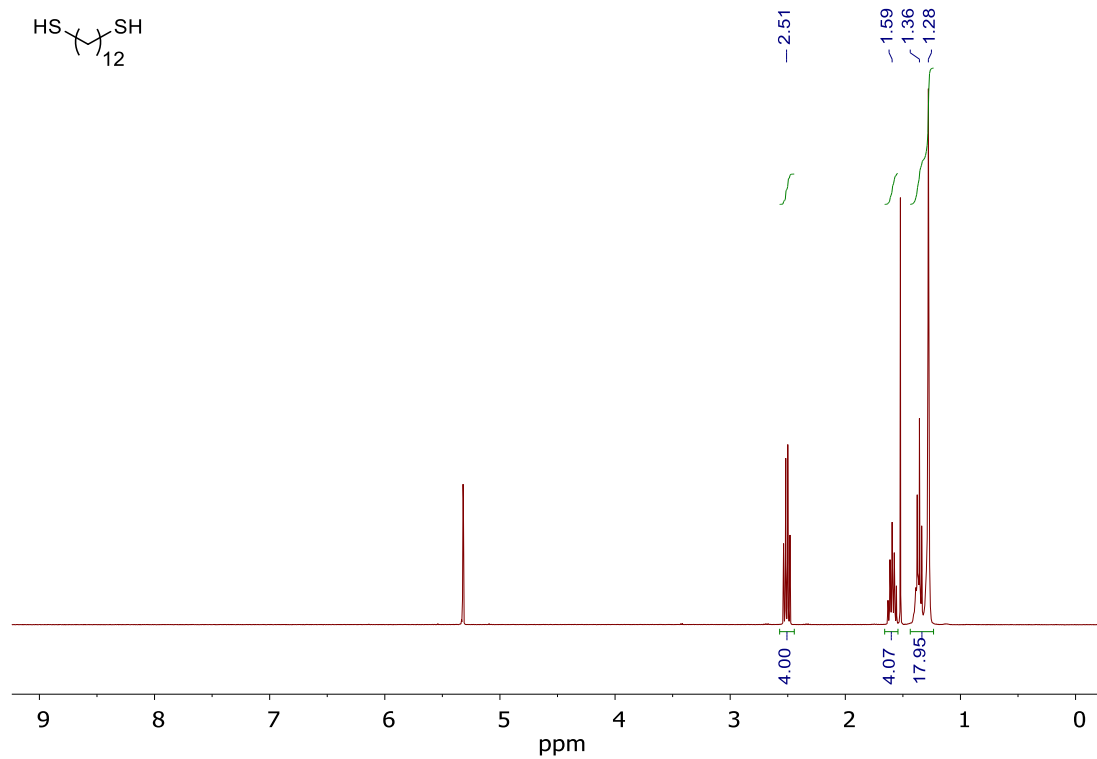


**Supplementary Figure 11.** XPS Sulfur 2p spectra (at  $15^\circ$ , average of 10 sweeps) of SAMs of monofunctional alkanes on Au prepared from: (a)  $C_{12}SH$  (blue) and (b)  $C_{12}SMe$  (black) solutions. All S 2p regions comprise a single doublet at  $\sim 162$  eV corresponding to gold-bound sulfur, again demonstrating that chemisorbed and physisorbed gold bonding cannot readily be distinguished using this technique for SAMs prepared from solution (see also discussion in manuscript). Spectra were aligned using the Au 4f XPS peaks.

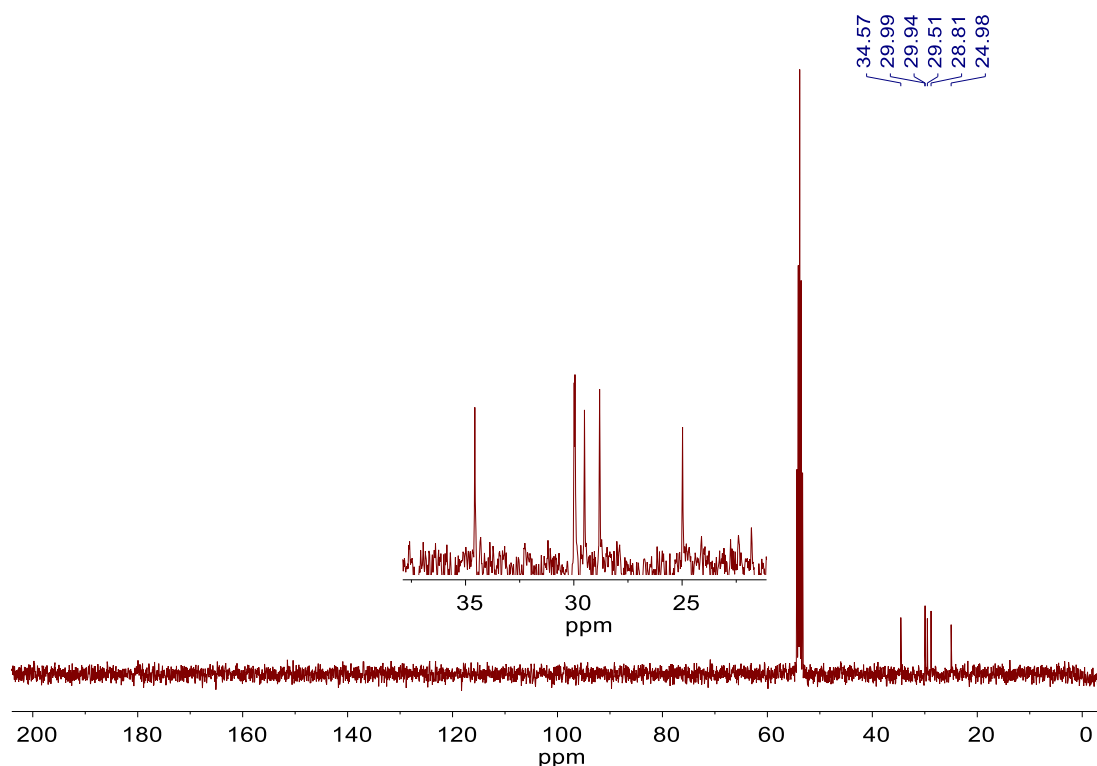


**Supplementary Figure 12.** Overlaid surface cyclic voltammograms for SAMs on gold working electrodes prepared from (a)  $\mathbf{C}_{12}\mathbf{SH}$  and (b)  $\mathbf{C}_{12}\mathbf{SMe}$  solutions. Measurements were conducted in 0.1 M KOH aqueous solution using Ag/AgCl reference and Pt counter electrodes, with potentials reported relative to Ag/AgCl. Both SAMs exhibit an initially passivated gold surface, where the first sweep to 0.6 V shows no features attributable to gold oxidation (orange voltammogram). In each case, subsequent sweeps to  $-1.4$  V reveal features below  $-1$  V that correspond to the reductive desorption of sulfur-bound species. These reduce in intensity with repeated cycling between 0.6 and  $-1.4$  V (orange arrows) and are commensurate with the increasing intensity of features attributable to gold oxidation (at 0.28 V) and reduction (at 0.12 V) (red arrows). After multiple sweeps these converge (red voltammogram), indicating all the SAM has been desorbed and the entire gold surface area is exposed to the electrolyte solution. SAM desorption appears to be more rapid in (b) compared to (a), as indicated by the relatively larger Au redox peaks in the second cycle (compare blue voltammograms for the second cycle). This is likely due to a less densely packed SAM for  $\mathbf{C}_{12}\mathbf{SMe}$  compared to  $\mathbf{C}_{12}\mathbf{SH}$ .

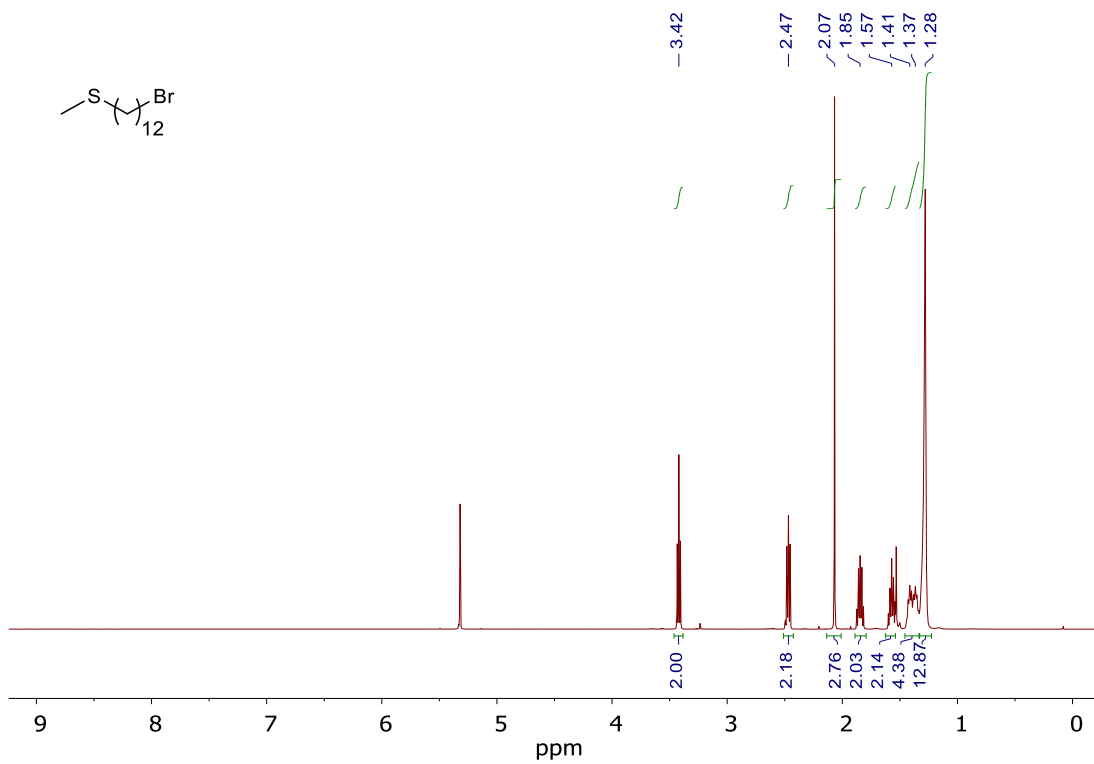
### 3. NMR Spectra



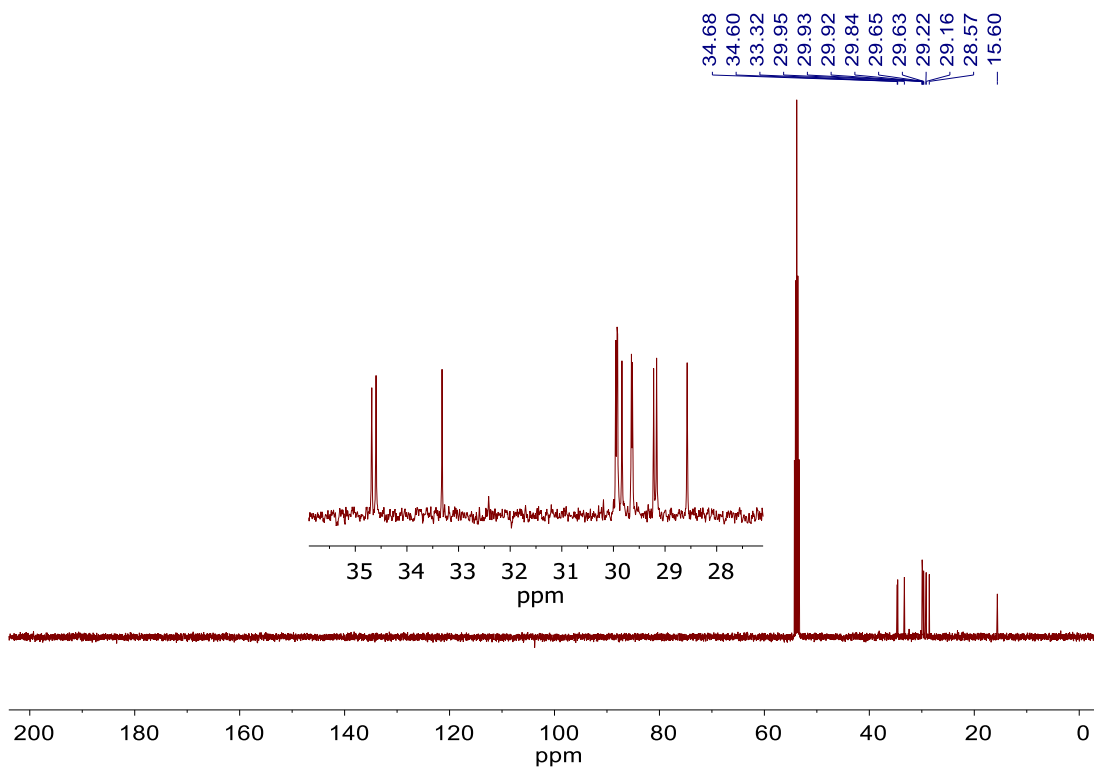
**Supplementary Figure 13.**  $^1\text{H}$  NMR spectrum of  $\text{C}_{12}(\text{SH})_2$  in  $\text{CD}_2\text{Cl}_2$ .



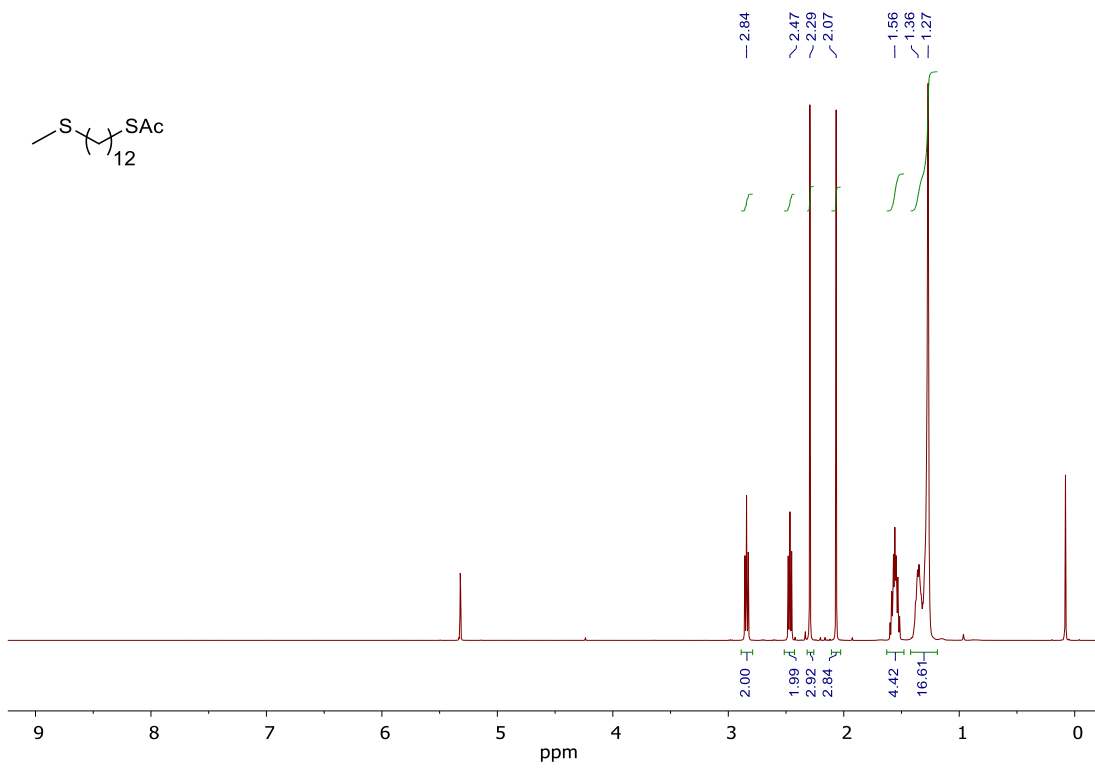
**Supplementary Figure 14.**  $^{13}\text{C}\{^1\text{H}\}$  NMR spectrum of  $\text{C}_{12}(\text{SH})_2$  in  $\text{CD}_2\text{Cl}_2$ .



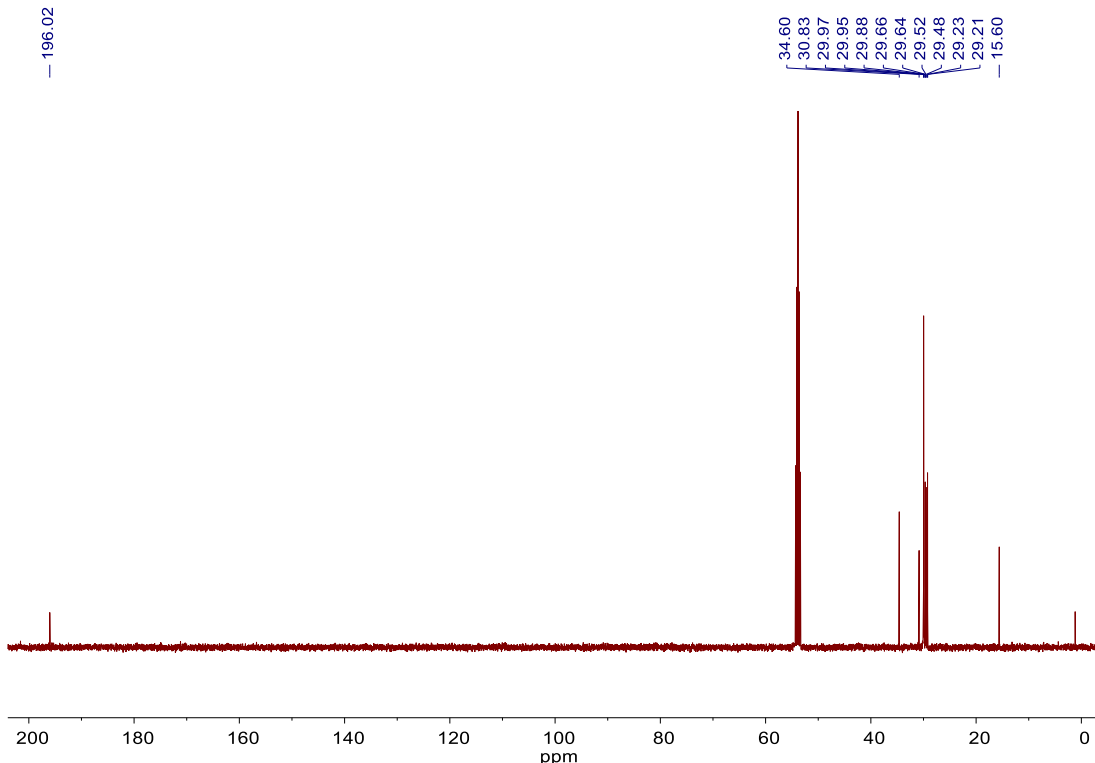
**Supplementary Figure 15.**  $^1\text{H}$  NMR spectrum of **1** in  $\text{CD}_2\text{Cl}_2$ .



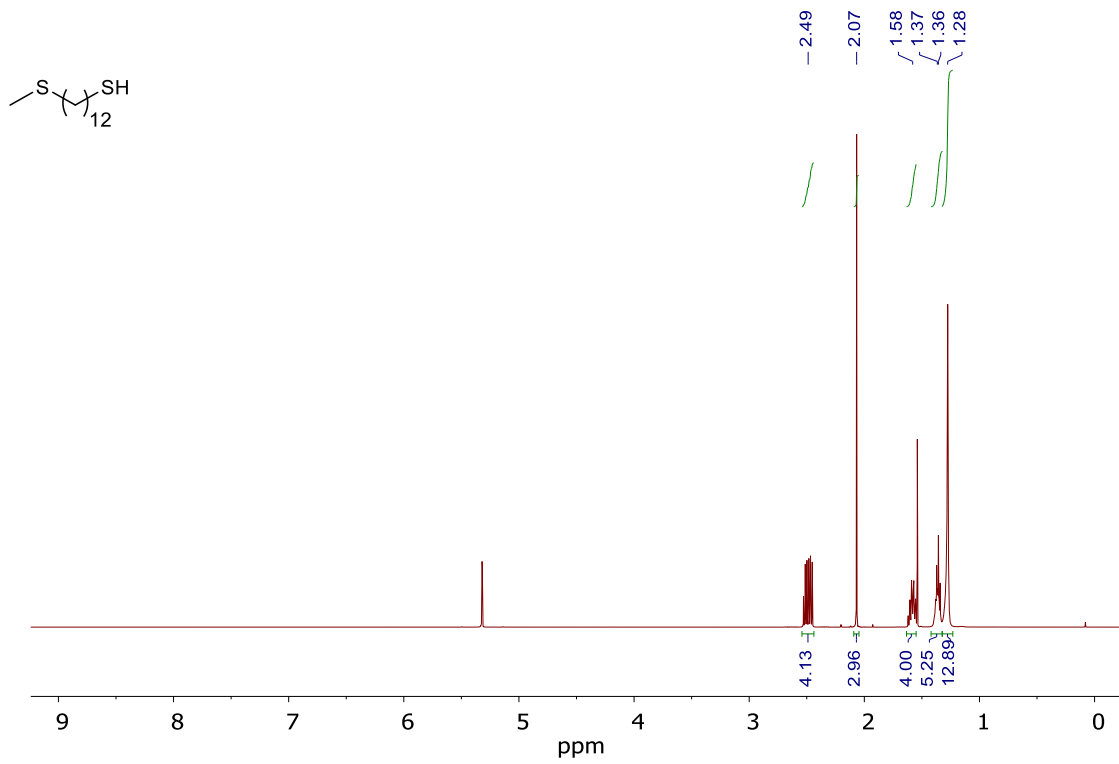
**Supplementary Figure 16.**  $^{13}\text{C}\{^1\text{H}\}$  NMR spectrum of **1** in  $\text{CD}_2\text{Cl}_2$ .



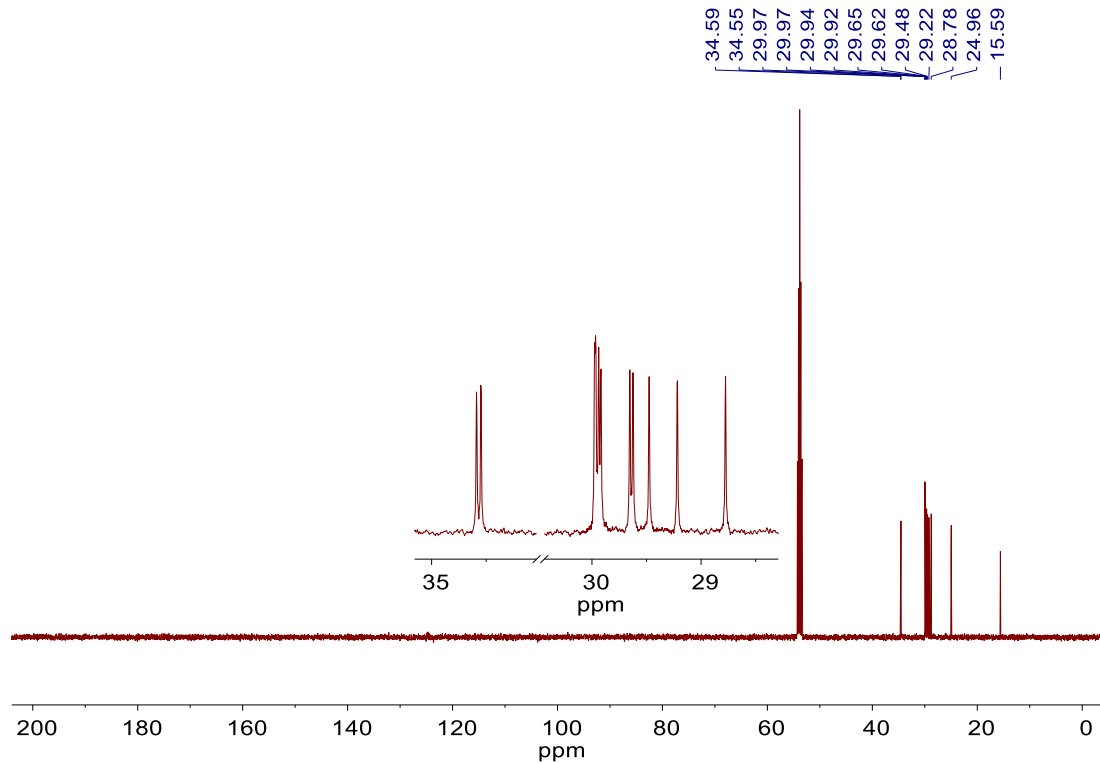
**Supplementary Figure 17.**  $^1\text{H}$  NMR spectrum of **2** in  $\text{CD}_2\text{Cl}_2$ .



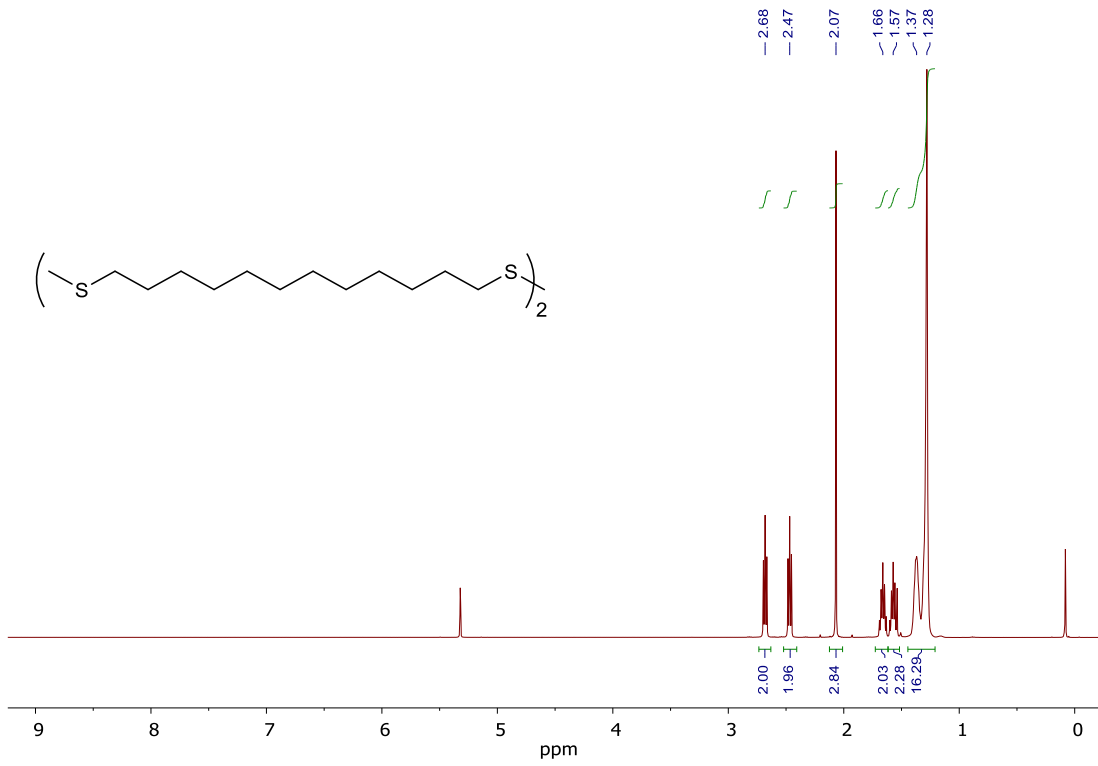
**Supplementary Figure 18.**  $^{13}\text{C}\{^1\text{H}\}$  NMR spectrum of **2** in  $\text{CD}_2\text{Cl}_2$ .



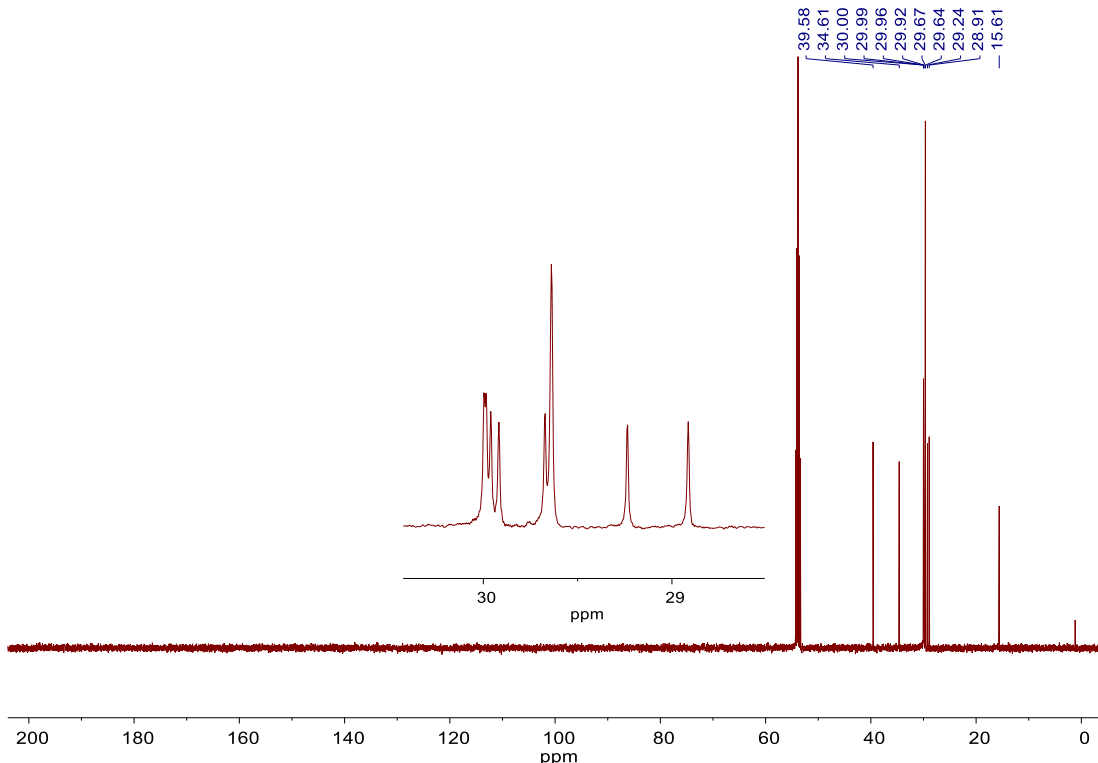
**Supplementary Figure 19.**  $^1\text{H}$  NMR spectrum of **C<sub>12</sub>(asym.)** in  $\text{CD}_2\text{Cl}_2$ .



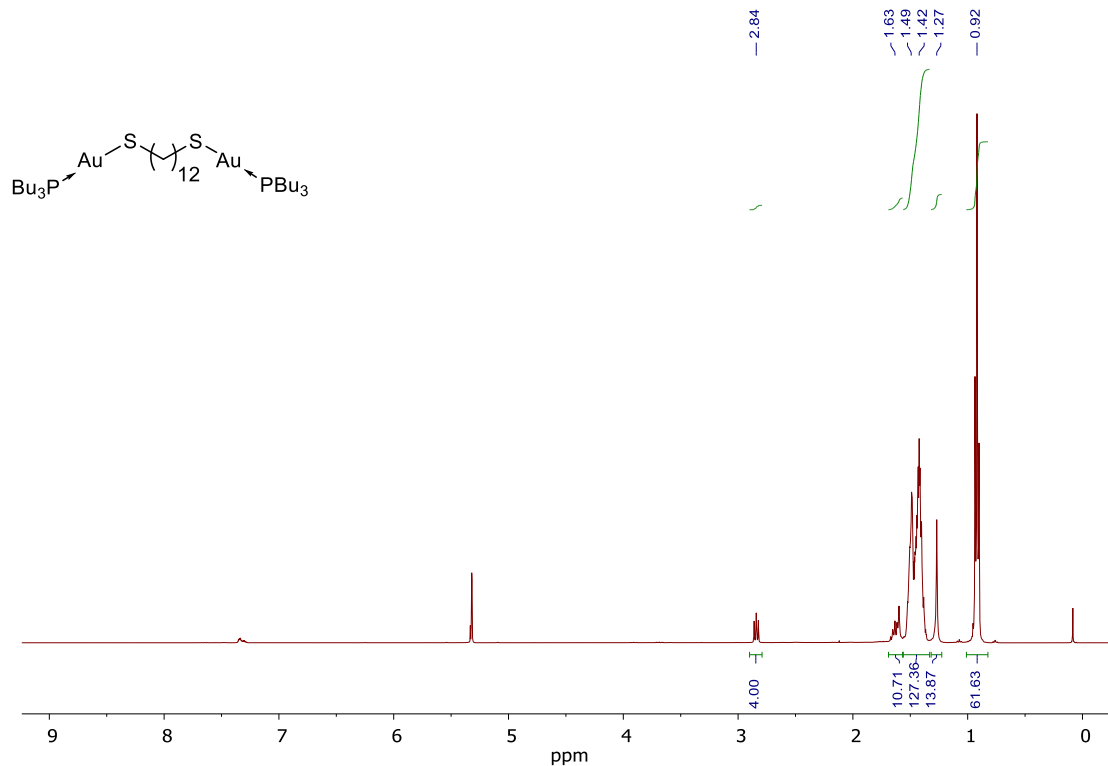
**Supplementary Figure 20.**  $^{13}\text{C}\{^1\text{H}\}$  NMR spectrum of **C<sub>12</sub>(asym.)** in  $\text{CD}_2\text{Cl}_2$ .



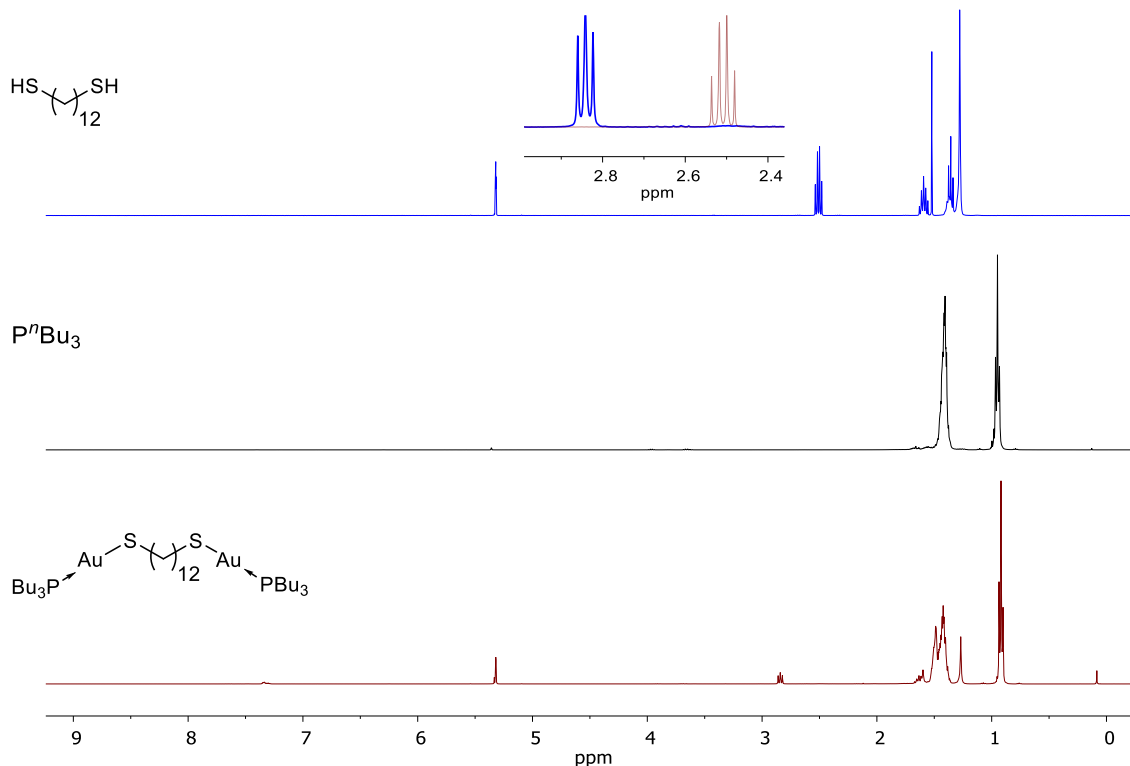
**Supplementary Figure 21.**  $^1\text{H}$  NMR spectrum of  $\text{C}_{12}(\text{diS})$  in  $\text{CD}_2\text{Cl}_2$ .



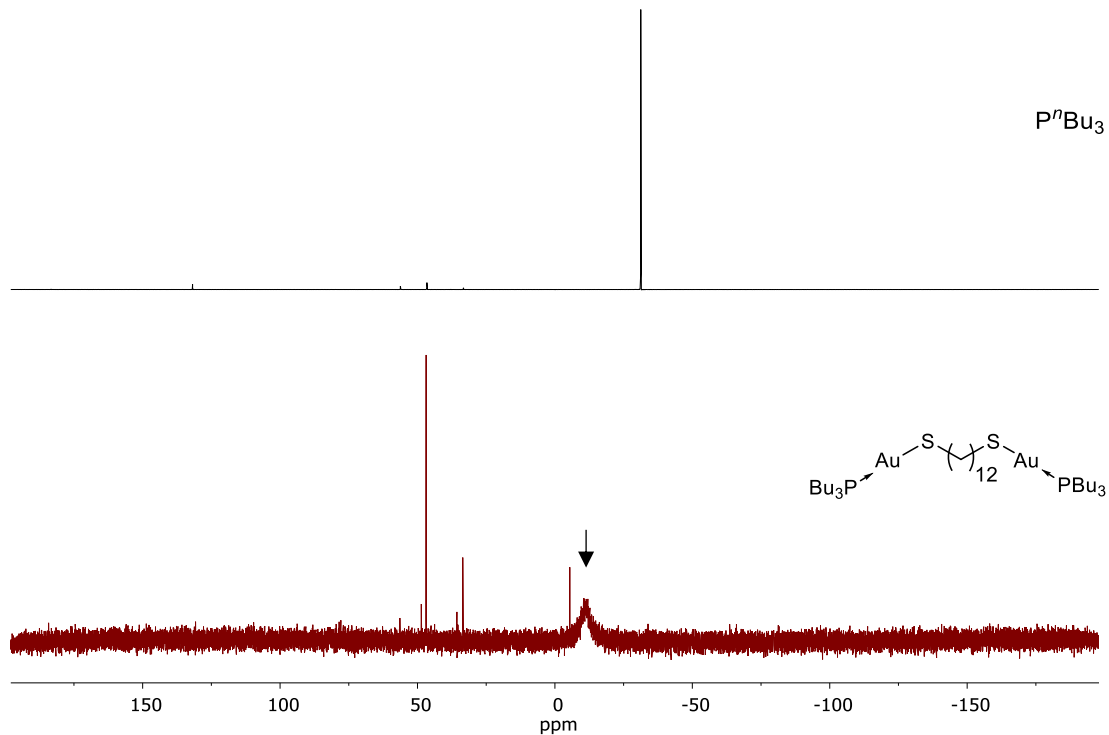
**Supplementary Figure 22.**  $^{13}\text{C}\{^1\text{H}\}$  NMR spectrum of  $\text{C}_{12}(\text{diS})$  in  $\text{CD}_2\text{Cl}_2$ .



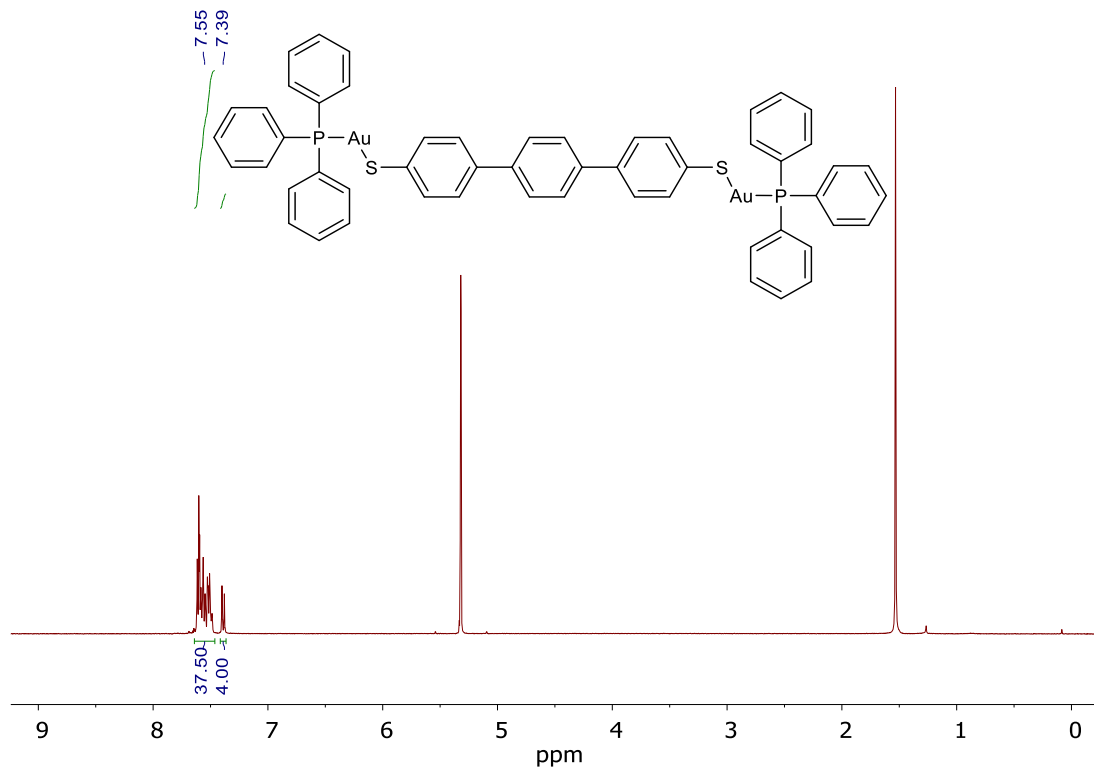
**Supplementary Figure 23.**  $^1\text{H}$  NMR spectrum of  $\text{C}_{12}(\text{SAuPBu}_3)_2$  in  $\text{CD}_2\text{Cl}_2$ .



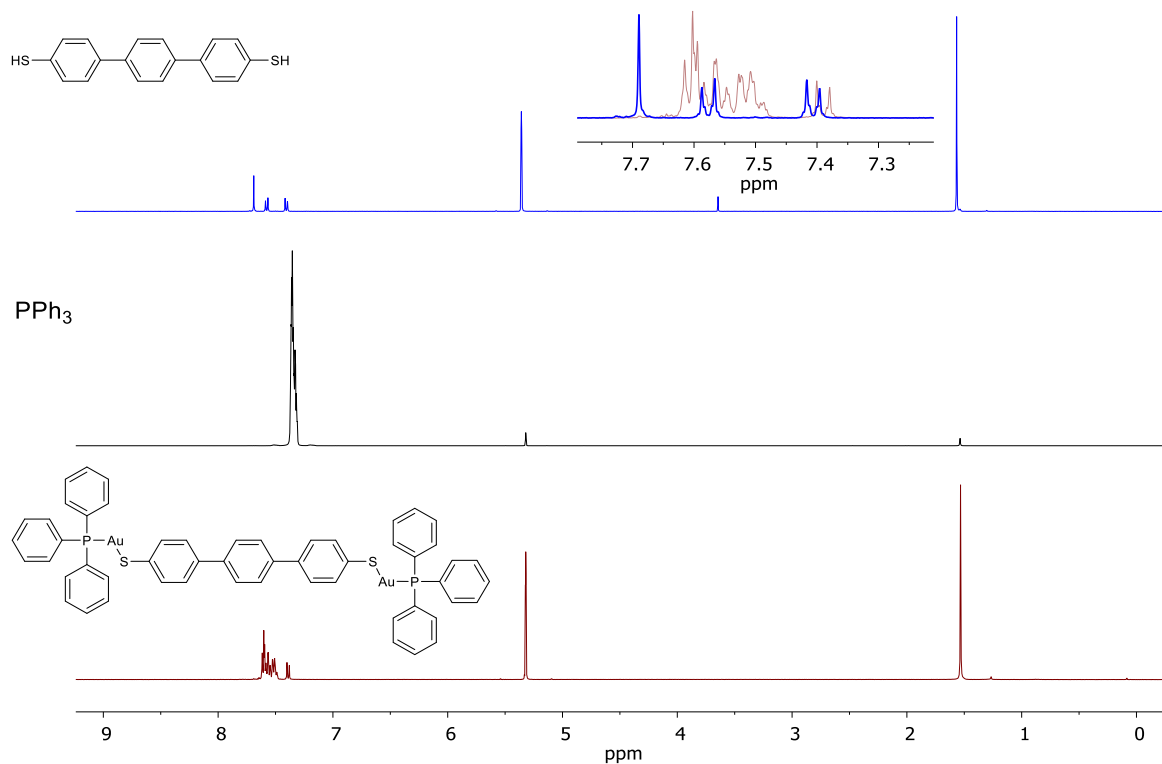
**Supplementary Figure 24.**  $^1\text{H}$  NMR spectra of  $\text{C}_{12}(\text{SH})_2$  (top),  $\text{P}^n\text{Bu}_3$  (middle) and  $\text{C}_{12}(\text{SAuPBu}_3)_2$  (bottom) in  $\text{CD}_2\text{Cl}_2$ . *Inset:* overlaid  $\text{S}-\text{CH}_2$  resonance for both compounds, showing a downfield shift and change from quartet to triplet splitting upon formation of the Au–thiolate bond.



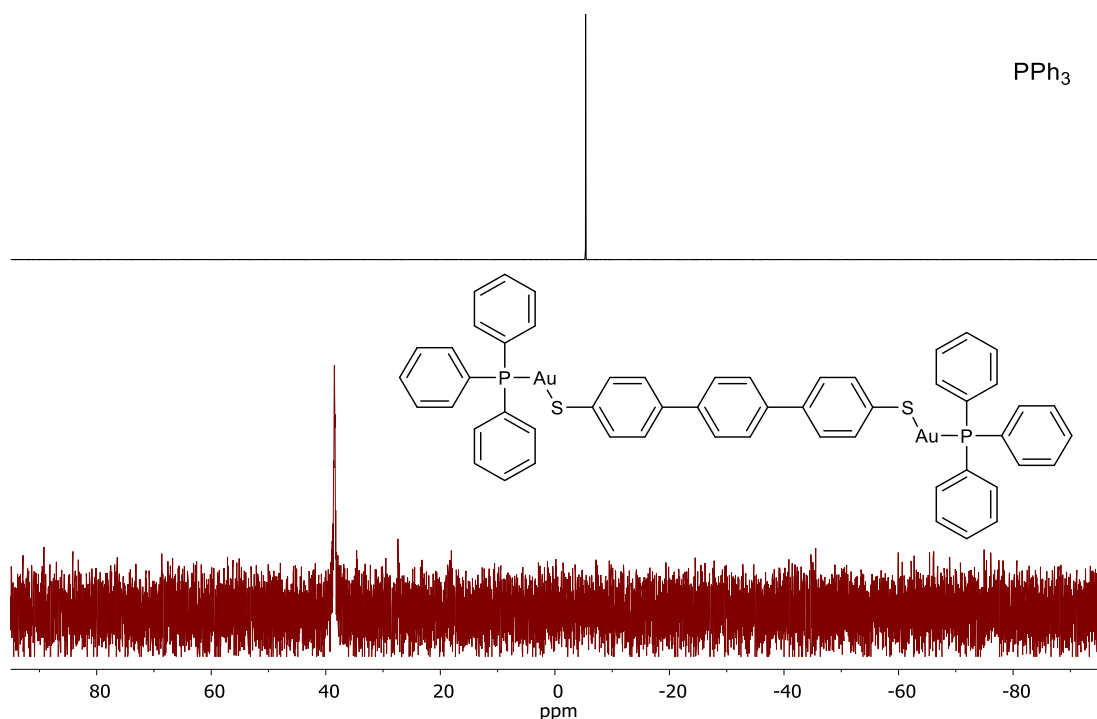
**Supplementary Figure 25.**  $^{31}\text{P}\{\text{H}\}$  NMR spectra of a commercial sample of  $\text{P}^n\text{Bu}_3$  (top) and  $\mathbf{C}_{12}(\text{SAuPBu}_3)_2$  (bottom) in  $\text{CD}_2\text{Cl}_2$ .



**Supplementary Figure 26.**  $^1\text{H}$  NMR spectrum of  $\mathbf{Ph}_3(\text{SAuPPh}_3)_2$  in  $\text{CD}_2\text{Cl}_2$ .



**Supplementary Figure 27.**  $^1\text{H}$  NMR spectra of  $[\text{Ph}_3(\text{SH})_2]$  (top) and  $\text{Ph}_3(\text{SAuPPh}_3)_2$  (bottom) in  $\text{CD}_2\text{Cl}_2$ . *Inset:* overlaid aromatic region for both compounds, showing there is no significant quantity of free  $\text{Ph}_3(\text{SH})_2$  present in the isolated sample of  $\text{Ph}_3(\text{SAuPPh}_3)_2$ .



**Supplementary Figure 28.**  $^{31}\text{P}\{\text{H}\}$  NMR spectrum of a commercial sample of  $\text{PPh}_3$  (top) and  $\text{Ph}_3(\text{SAuPPH}_3)_2$  (bottom) in  $\text{CD}_2\text{Cl}_2$ .

#### 4. References

1. Venkataraman, L. *et al.* Single-Molecule Circuits with Well-Defined Molecular Conductance. *Nano Lett.* **6**, 458–462, (2006)
2. Hegner, M., Wagner, P. & Semenza, G. Ultralarge atomically flat template-stripped Au surfaces for scanning probe microscopy. *Surf. Sci.* **291**, 39–46, (1993)
3. Weiss, E. A. *et al.* Si/SiO<sub>2</sub>-Templated Formation of Ultraflat Metal Surfaces on Glass, Polymer, and Solder Supports: Their Use as Substrates for Self-Assembled Monolayers. *Langmuir* **23**, 9686–9694, (2007)
4. Li, H. *et al.* Extreme Conductance Suppression in Molecular Siloxanes. *J. Am. Chem. Soc.* **139**, 10212–10215, (2017)
5. Scullion, L. E., Leary, E., Higgins, S. J. & Nichols, R. J. Single-molecule conductance determinations on HS(CH<sub>2</sub>)<sub>4</sub>O(CH<sub>2</sub>)<sub>4</sub>SH and HS(CH<sub>2</sub>)<sub>2</sub>O(CH<sub>2</sub>)<sub>2</sub>O(CH<sub>2</sub>)<sub>2</sub>SH, and comparison with alkanedithiols of the same length. *J. Phys.: Condens. Matter* **24**, 164211, (2012)
6. Polster, J. & Schieberle, P. Structure-Odor Correlations in Homologous Series of Alkanethiols and Attempts To Predict Odor Thresholds by 3D-QSAR Studies. *J. Agric. Food Chem.* **63**, 1419–1432, (2015)
7. Li, H. *et al.* Electric Field Breakdown in Single Molecule Junctions. *J. Am. Chem. Soc.* **137**, 5028–5033, (2015)
8. Kirihara, M. *et al.* A Mild and Environmentally Benign Oxidation of Thiols to Disulfides. *Synthesis* **2007**, 3286–3289, (2007)
9. Atsushi, S. *et al.* Solvent Diversity in the Preparation of Alkanethiol-capped Gold Nanoparticles. An Approach with a Gold(I) Thiolate Complex. *Chem. Lett.* **39**, 319–321, (2010)
10. Forward, J. M., Bohmann, D., Fackler, J. P. & Staples, R. J. Luminescence Studies of Gold(I) Thiolate Complexes. *Inorg. Chem.* **34**, 6330–6336, (1995)
11. Monzittu, F. M. *et al.* Different emissive properties in dithiolate gold(I) complexes as a function of the presence of phenylene spacers. *Dalton Trans.* **43**, 6212–6220, (2014)
12. Quek, S. Y. *et al.* Amine–Gold Linked Single-Molecule Circuits: Experiment and Theory. *Nano Lett.* **7**, 3477–3482, (2007)
13. Paulsson, M., Krag, C., Frederiksen, T. & Brandbyge, M. Conductance of Alkanedithiol Single-Molecule Junctions: A Molecular Dynamics Study. *Nano Letters* **9**, 117–121, (2009)